LAIDLAW SCHOLARISHIP REPORT PAPER

DEFINING THE GEOTECHNICAL PROPERTIES OF LUNAR SIMULANT REGOLITH

Freya GARRIGAN
MEng Engineering and Architectural Design student
In collaboration with the Geotechnics Laboratory and Civil, Environmental and Geomatic Engineering Department

TABLE OF CONTENTS

Note:

The term "regolith" is used throughout this guide to emphasise the Moon's unique surface material, distinguishing it from the more Earth-associated term "soil" used during the Apollo era. While both terms refer to the same unconsolidated surface material, "soil" is retained in historical contexts and when referring to Apollo samples but does not contain any organic material and is not formed through biologic or chemical means (Noble S, 2020).

Additionally, the word "Morphologi" refers to the machine used for particle shape characterisation whereas "Morphology" refers to the physical structure of the particle being analysed.

1. INTRODUCTION

As interest grows in establishing a sustained human presence on the Moon, attention is turning to how lunar surface materials will behave when supporting engineered structures. Upcoming missions, including NASA's Artemis programme, plan to develop installations near the Moon's south pole, prompting urgent research into the interaction between regolith and infrastructure.

Designing reliable systems for habitation, mobility, and construction requires accurate modelling of regolith mechanics under lunar conditions. Due to the scarcity and preservation requirements of returned lunar material, terrestrial simulants are used for testing instead. Whilst these simulants aim to replicate both the mineralogical composition and physical particle characteristics of Apollo retrieved lunar soils, limited information is known on the geotechnical properties. This study investigates several such simulants, categorised in table 2. This includes Hostun sand, a well-characterised French quartz sand used for baseline comparison, and high-fidelity lunar regolith simulants developed by the Exolith Lab.

1.1 Lunar surface

1.1.1 General

Lunar regolith is a fine-grained, unconsolidated layer of soil-like material that blankets the Moon's surface, formed through billions of years of mechanical breakdown by micrometeoroid impacts, solar wind sputtering, and thermal fatigue (Carrier et al., 1991), as seen in figure 1. In the absence of an atmosphere, these physical processes dominate regolith formation, resulting in highly angular, irregular particles with sharp edges (McKay et al., 1991). Its depth varies significantly, from about 4–5 m in basaltic maria regions to over 10 m in the older, heavily cratered highlands (Heiken et al., 1991).

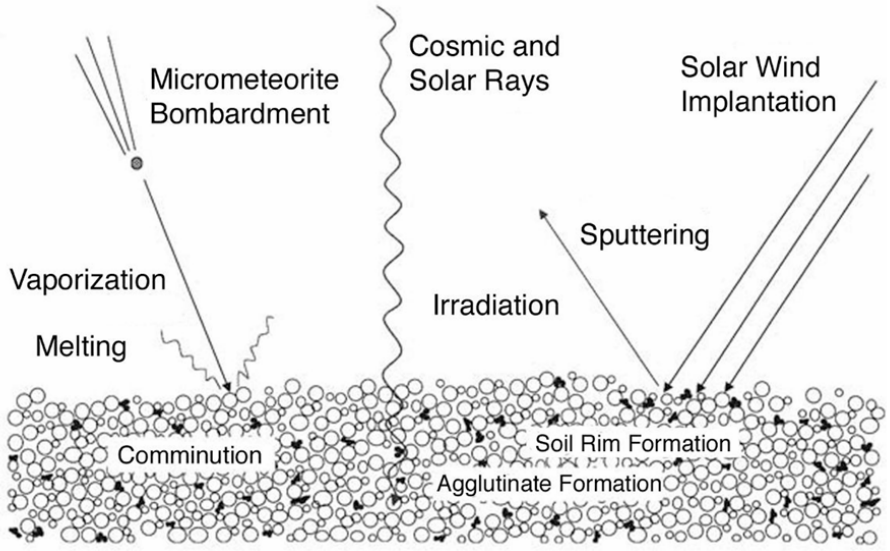

Figure 1. Illustration of the varying weathering processes on the lunar soil contributing to the breakdown of regolith into finer particle fractions (Noble S, 2020)

1.1.2 Mineral composition and distribution

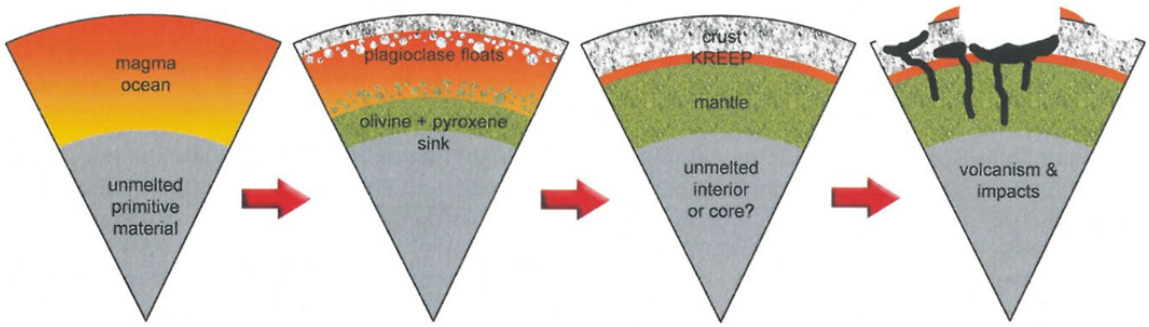

Figure 2. Diagram illustrating the timeline of the lunar magma ocean hypothesis leading to the distribution of basalt and anorthosite crust across the surface (NASA,2024)

The mineral composition of lunar regolith varies with location and geological history. Mare soils, derived from basaltic lava flows, are rich in pyroxene, olivine, and plagioclase, often with significant amounts of ilmenite (TiO_2-bearing) (Papike et al., 1998). By contrast, highland soils originate from anorthosite crust, consisting predominantly of plagioclase feldspar with minor pyroxene and olivine (see figure 3) with the South pole originating largely from anorthosite as well. These have been distributed across the surface by volcanic activity and meteor impacts as seen in figure 2.

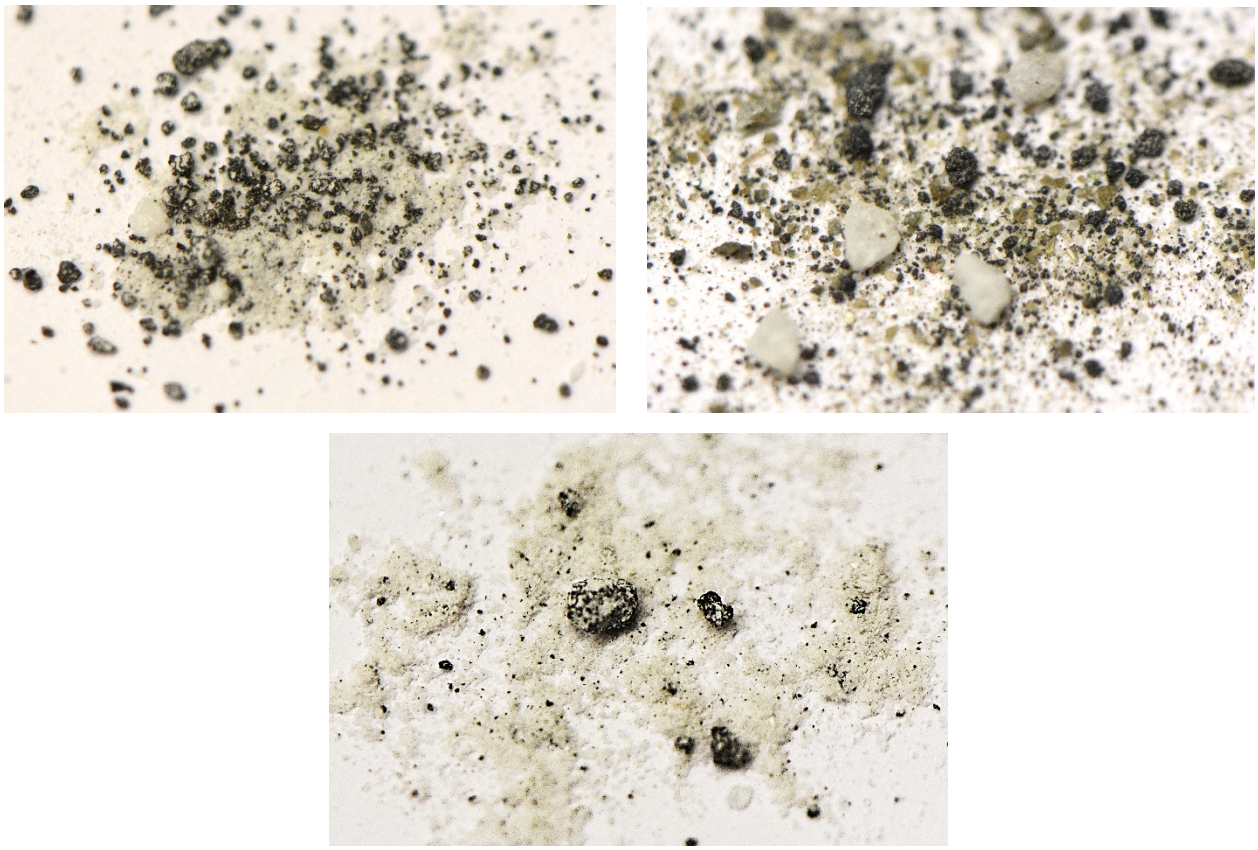

Figure 3. (Left) Lunar highlands LHS simulant and (Right) Lunar Mare simulant, (Bottom) Lunar South pole simulant, all from Exolith labs (Garrigan F, 2025)

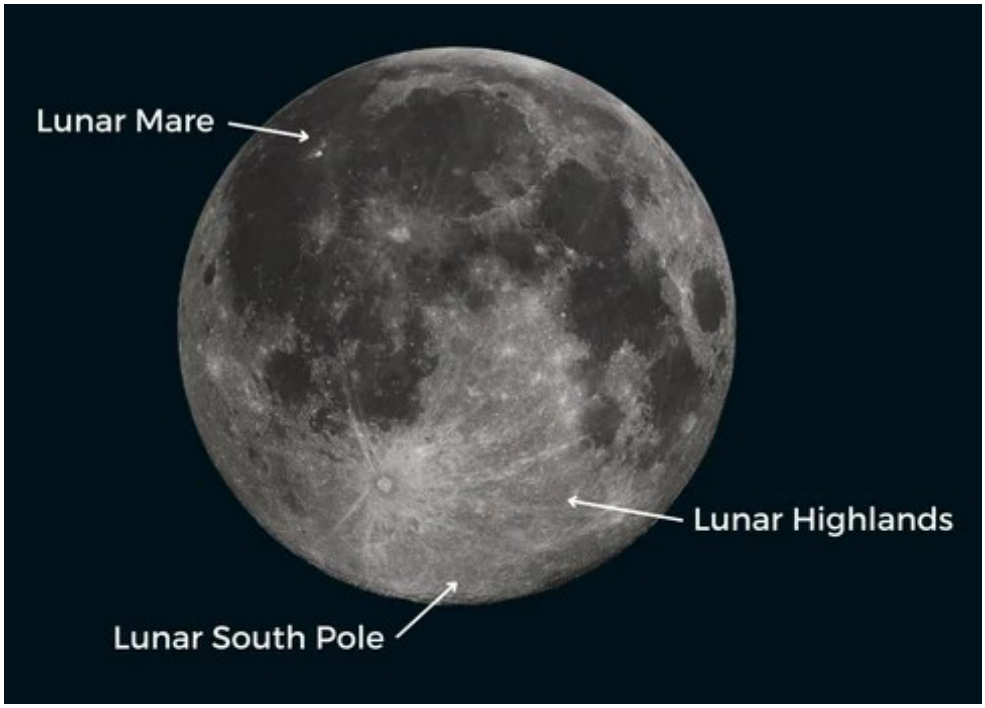

Figure 4. Illustration depicting examples of lunar regions used for simulant type separation (Exolith labs, 2024)

A distinguishing feature of lunar soil is the presence of agglutinates, glassy, welded aggregates of mineral and rock fragments formed through micrometeoroid impacts, see figure 4. Agglutinates can make up 50 to 70% of mature regolith, (see figure 4) characterised traditionally by its nanophase iron and agglutinate content (Noble S,2020) , contributing to its complex mechanical properties (Taylor et al., 2005).

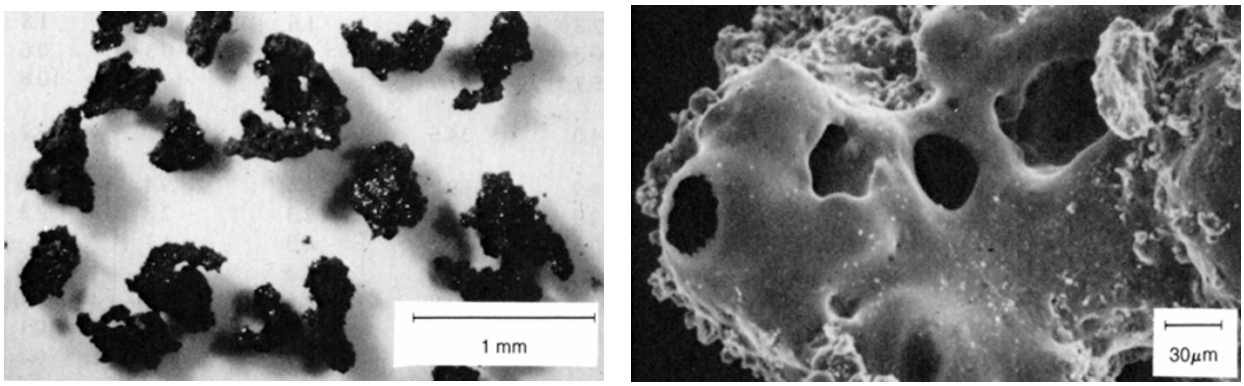

Figure 4. (Left) Optical microscope photograph of a number of agglutinated from Apollo 11 (Right) SEM view of a glassy agglutinate surface, showing vesicular structure. Small mounds and trains of metallic Fe are visible as bright spots that occur over the entire glassy surface (McKay et al,1991)

Table 1 breaks down the mineralogy of the 3 main categories of lunar regolith into its main constituent parts. To obtain these distributions, NASA averaged the % weight of the mineral components of multiple samples retrieved from across the Apollo missions. For this report I have chosen to focus on the low-Ti bearing Mare regolith which is the most replicated form of Mare soil by the simulant market.

Table 1. Mineralogy content of lunar regions averaged from retrieved Apollo samples

Component	***Highlands (wt.%)***	***Mare (low-Ti) (wt.%)***
Anorthosite (plagioclase)	59.05	28.97
Glass (amorphous content)	27.77	32.98
Ilmenite	0.15	3.86
Olivine	5.11	6.89
Pyroxene	7.92	24.97

1.2 Lunar simulants

Though lunar regolith contains the same major rock-forming elements and minerals as Earth, found in rocks like anorthosite and basalt, its surface remains unlike any terrestrial substrate. As a result, we can produce Earth-based simulants with similar components, however due to the variety of regolith types found across the surface, simulants are split by surface for better replication.

Table 2. Mineralogy content of the 5 categories

Component	***LHS (wt.%)***	***LHS-25A (wt.%)***	***LMS (low-Ti) (wt.%)***	***LSP (wt.%)***	***Hostun (wt.%)***
Anorthosite (plagioclase)	74.4	55.8	19.8	90	0
Glass-rich basalt	24.7	18.5	32.0	10	0
Ilmenite	0.4	0.3	4.3	0	0
Olivine	0.2	0.15	11.1	0	0
Pyroxene	0.3	0.2	32.8	0	0
Glass agglutinates	0	25	0	0	0
Quartz	0	0	0	0	100

The first 4 simulants in table 2 are classified as hi-fi replicas of lunar soil from Exolith labs and are marketed as accurately capturing the texture of lunar regolith and particle size distribution by combining both mineral and rock fragments (Exolith labs, 2024) however only LHS-25A contains the glass agglutinates found in real lunar samples, aiming to replicate an intermediately mature Lunar highlands Regolith. All minerals used for the simulants are retrieved from the same locations, therefore the only simulants are distinguished only by their wt% and particle distribution. Hostun sand on the other hand is marketed as a cheaper and more accessible alternative, used more frequently when bulk quantities are required for testing rover wheels or scenes.

Table 3. Contains simulant type and its visual appearance with 10mm cube

Sample type	***Image***
LHS highland simulant	
LHS-25A highland agglutinated simulant	
LMS mare simulant	
LSP south pole simulant	
Hostun sand	

2. LITERATURE REVIEW

2.1 Normal loading

Normal (axial) loading will be conducted on particles from the simulants, either with the load applied directly to one particle by a platen or via contact with another particle of the same mineralogy. A contact theory developed by Hertz in 1882 is often used, with particles modelled as smooth spheres and displacements that occur due to normal loading assumed to be highly localised to the contact area. The formula for the radius of contact area (a_h) is given in equation 1:

$$a_h = \left(\frac{3NR}{4E^*}\right)^{\frac{1}{3}} \quad (1)$$

Where N is the normal force applied to the particle(s) [N], R is the equivalent radius given using equation 1.1 [m], E is the equivalent elastic modulus given using equation 1.2 [Pa]*

$$\frac{1}{R} = \frac{1}{R_1} + \frac{1}{R_2} \quad (1.1)$$

Where R is the equivalent radius [m], and R_1 and R_2 are the radii of the circles that circumscribe the arc of the contact point [m], see figure 5 for an example of circle used

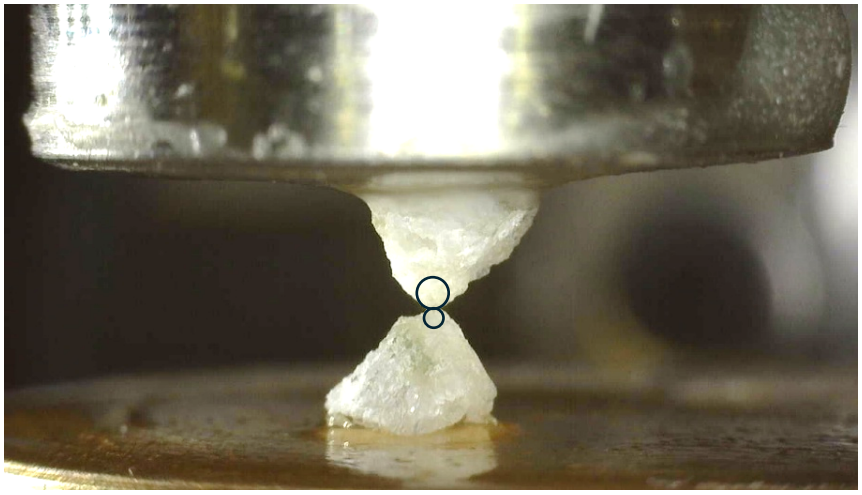

Figure 5. Image of circle used to collect radius of circle that circumscribes the arc of the contact point of the particle

$$\frac{1}{E^*} = \frac{(1-\nu_1^2)}{E_1} + \frac{(1-\nu_2^2)}{E_2} \quad (1.2)$$

Where E^* is the equivalent elastic modulus [Pa], υ_1 and υ_2 are the poisons ratios of the two materials[nd], and E_1 and E_2 are the Young's moduli of the materials [Pa]

The displacement of the force due to the load can then be calculated using equation 2:

$$\delta = \frac{a_h^2}{R} \quad (2)$$

Where δ is the displacement of the centre points of the sphere relative to the other [m], a_h is the radius of the contact area [m], R is the equivalent radius [m]

2.1.1 Normal loading with roughness

To model the behaviour of the particles more realistically under loading, we can adjust the hertz model using Greenwood et al.'s (1984) introduction of a non-dimensional surface roughness parameter (α) to account for the sphericity and roughness of the particles. α is calculated using equation 3:

$$\alpha = \frac{S_q R}{a_h^2} \quad (3)$$

Where a_h is the contact radius determined in eq 1 [m], S_q is the combined roughness determined in eq 3.1, R is the equivalent radius [m]

$$S_q = \left(S_{q_1}^{\ 2} + S_{q_2}^{\ 2}\right)^{\frac{1}{2}} \quad (3.1)$$

Where S_{q_1} and S_{q_2} are the RMS roughness of the two materials

Using α we can then determine a*, the equivalent contact area accounting for the RMS roughness proposed by Yimsiri and Soga in 2000. a* is defined by equation 4:

$$\boldsymbol{a^* = \left(\frac{-2.8}{\alpha + 2} + 2.4\right) \cdot a_h} \quad \textbf{(4)}$$

Where α is the roughness parameter from equation 3

Subsequently, due to the roughness caused by the interlocking of the asperities at the contact area, the equivalent contact area is larger than that of the original Hertz model. Hence, the new displacement (δ^*) is defined by equation 5:

$$\boldsymbol{\delta^* = \frac{2a^{*2}}{R}} \quad \textbf{(5)}$$

Where a is the roughness parameter defined in equation 3, and R is the equivalent radius defined in equation 1.1*

2.2 Particle strength and Weibull statistics

Measuring the strength of individual particles in lunar regolith simulant provides critical insight into the mechanical behaviour of extraterrestrial soils, where particle breakage can significantly influence load-bearing capacity, compaction, and long-term stability in low-gravity environments. Following research from Hiramatsu and Oka (1966) and Cavarretta (2009) we can define particle strength (σ_f) by equation 6:

$$\boldsymbol{\sigma_f = \frac{0.9N}{d^2}} \quad \textbf{(6)}$$

Where N is the peak load applied to the particle at breakage [N], d is the equivalent diameter of the particle defined by equation 6.1

Since the particles are not spherical, Wang and Coop (2006) suggested calculating d by finding the geometric mean of the particle defined by equation 6.1:

$$\boldsymbol{d = (d_1 \cdot d_2)^{\frac{1}{2}}} \quad \textbf{(6.1)}$$

Where d_1 and d_2 are the minor and intermediate diameters of the particles

An example of how d_1 and d_2 are measured can be seen in figure 6, also referred to as L (large), I (intermediate) and S (small) by Sneed and Folk,1958.

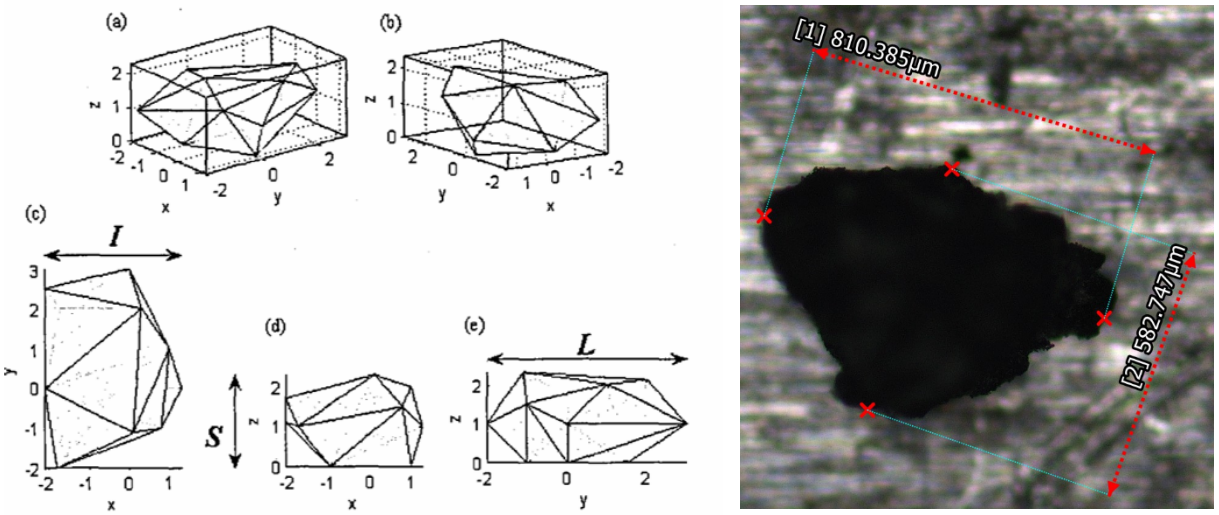

Figure 6. (Left) definition of dimensions parameters used throughout paper (Cavarretta,2009) , (right) image of d_1 and d_2 from Keyence microscope

2.2.1 Probability of survival

To determine based on experimental data how likely a particle is to survive past a specific peak load, Weibull (1951) suggested defining a property of the particles called the characteristic strength (σ_0). Based on a cumulative distribution of Probability of a particle surviving crushing [%] vs Applied stress [Mpa] he defined σ_0 as the stress at which only 37% of the particles would survive.

$$P_s = \frac{n}{x} \cdot 100 \tag{7}$$

Where n is the position of the particle in the list of data, ordered from highest peak load to lowest peak load, x is the total number of samples in the experiment

Using σ_0 and P_s a particles chance of survival, a graph of $\ln(\ln(1/P_s))$ against $\ln(\sigma/\sigma_0)$ can be plotted and the gradient of the line formed, m, is the Weibull moduli of the sand.

2.3 Particle failure modes

A number of tests that will be carried out on the regolith simulants will be destructive, therefore its important to predefine the failure modes of the particles under load into categories; these can provide deeper insight into the difference in peak load for example, of each failure mode and if one mineral is more predisposed to a certain mode than another. Wang and Coop (2016) defined 5 failure modes (see table 4) when testing sand in a uniaxial loading frame which will also be used for this paper.

Table 4. Fracture modes of particles under normal loading, images from Wang and Coop,2016

Mode and description	***Visualisation***
1. Splitting (S) The particle fractures into two or three major pieces, without generating numerous small fragments	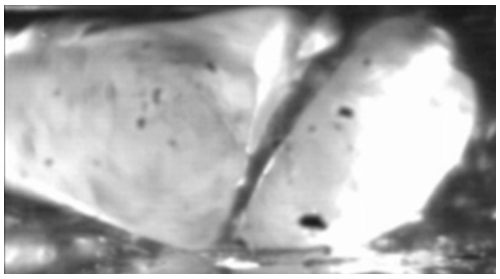
2. Explosive (E) The particle suddenly shatters into numerous small fragments.	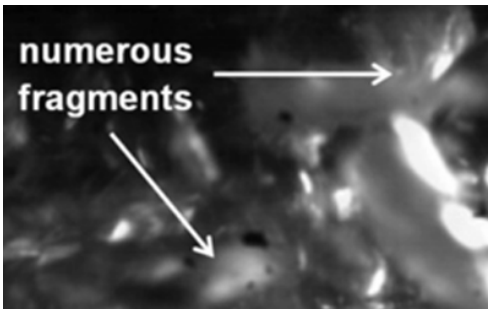
3. Chipping (C) A minor fragment of the particle chips of but does not cause critical failure.	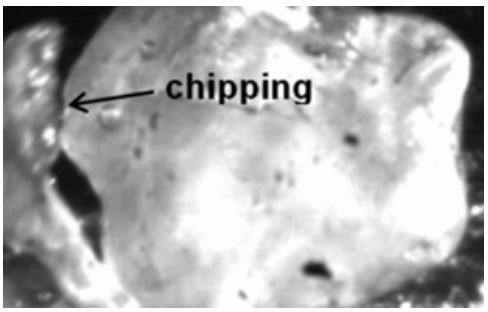
4. Mixed (M) As implied by the title, it is a mixed fracture type merging split and explosive patterns but more characteristic to splitting. Traditionally, A smaller fragment shatters into small pieces, while a larger one remains lodged between the platens.	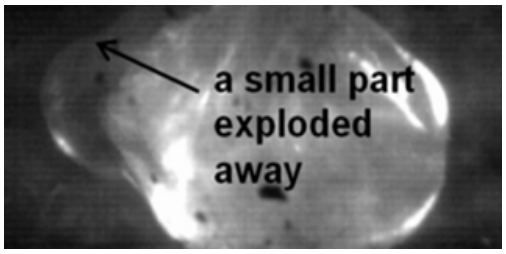
5. Core remaining (CR) Particles with fewer initial flaws, such as quartz sands, often exhibit a failure mode where the outer layer shatters into small fragments, leaving behind a column-shaped core.	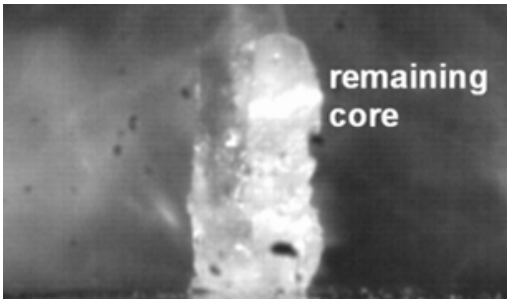

2.4 Particle morphology

Alongside a particles physical properties such as strength, shape parameters can also be quantitively measured and used to compare properties such as how spherical a particle is or how smooth it is. These parameters are useful for accurate DEM (Discrete Element Modelling) and predicting how the particle interacts with other particles in bulk under loading; such as a rough particles tendency to interlock.

2.4.1 Shape parameters

These parameters also span across the micro (such as RMS roughness), meso (such as roundness) and macro (such as sphericity and circularity). Table 5 lists the shape parameters that will be analysed in this paper.

Table 5. List of common particle shape parameters and their description

Parameter	Description
Circular equivalent diameter	Described as the diameter of a circle with the same projected area as the particle when viewed in a specified orientation
Convexity	Described as the particles actual outline to the outline of the smallest convex shape that can completely enclose it
Circularity	Often used as a 2D proxy for 3D sphericity, it is described as the ratio of the radius of the maximum inscribed circle of the outside of the particle to the minimum circumscribed circle that fits inside the particle. Measured from 0 to 1.
Aspect ratio	Described as the ratio between the large and intermediate diameters of the particle
Sphericity	Describes how similar a particles shape is to a sphere from 0 to 1. 1 being perfect sphere.
Roundness	Describes how angular a particle is. Measured by taking the ratio of the average radius of inscribed circles of each corner and the maximum inscribed circle of the particle.
RMS Roughness (sq)	Described as the standard deviation of the square from a reference line, which is the particles main body shape in this case.

2.4.2 Particle size

Particle size is another important parameter. Using the particles CE diameter, a cumulative particle size distribution can be created to define a samples average size and its variance. From this, a sample can be categorised by how fine its particle fractions are using the Wentworth scale seen in table 6, categorised in 1922. Generally the samples collected from Apollo predominantly consisted of the silt category, with about 20% classified as 1mm and above.

Table 6. Wentworth grain size classification 1922

Millimeters (mm)	Micrometers (μm)	Wentworth Size Class (with common sediment name)	
		Boulder	Gravel
256		Cobble	
64		Pebble	
4		Granule	
2		Very Coarse Sand	Sand
1		Coarse Sand	
1/2 (0.50)	500	Medium Sand	
1/4 (0.25)	250	Fine Sand	
1/8 (0.125)	125	Very Fine Sand	
1/16 (0.0625)	63	Silt	Mud
1/256 (0.0039)	3.9	Clay	

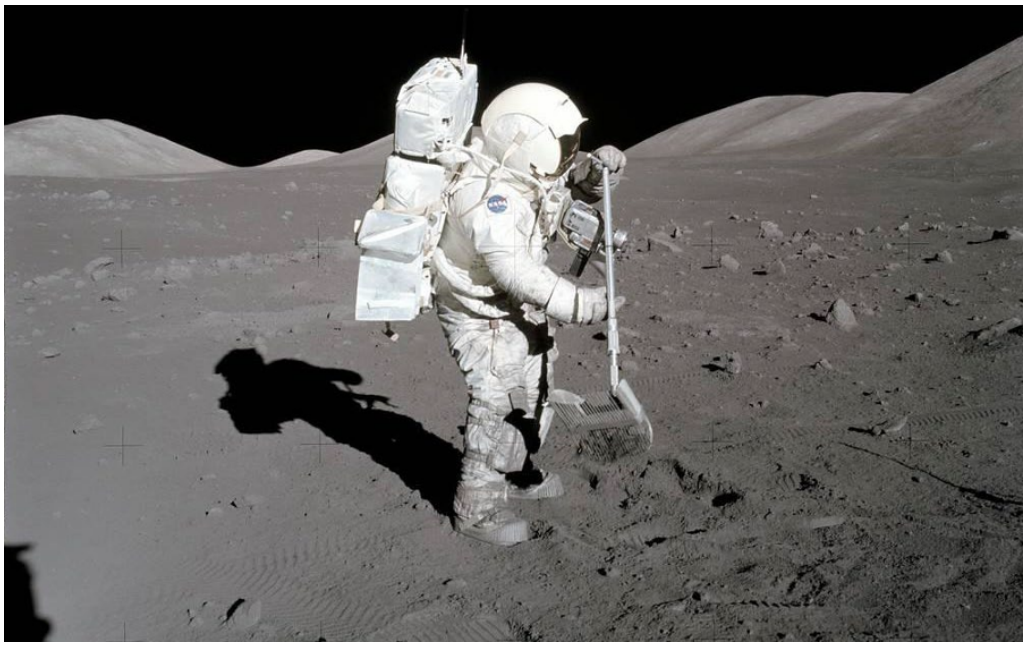

Figure 7. Photo from Apollo 17 shows an astronaut collecting a sample of lunar regolith. The terrain appears silty with scattered boulders (NASA, 2024)

2.4.3 Pixel requirements

It is worth noting that as exploded by Sun et al 2019 some fine level parameters such as convexity and circularity require quite large minimum pixel levels to be reliably measured. Therefore when analysing the particle morphology data the pixels in the particles must be taken into account, particularly due to the presence fine silty fractions in the regolith which may not be appropriately captured at low magnifications.

3. EQUIPMENT AND SET UP

3.1 Small uniaxial loading frame

The first experiment carried out on the particles is the crushing of a single particle between two metal platens, creating two contact points with the particle with a uniaxial load applied until failure. Figure 8 depicts the loading frame used.

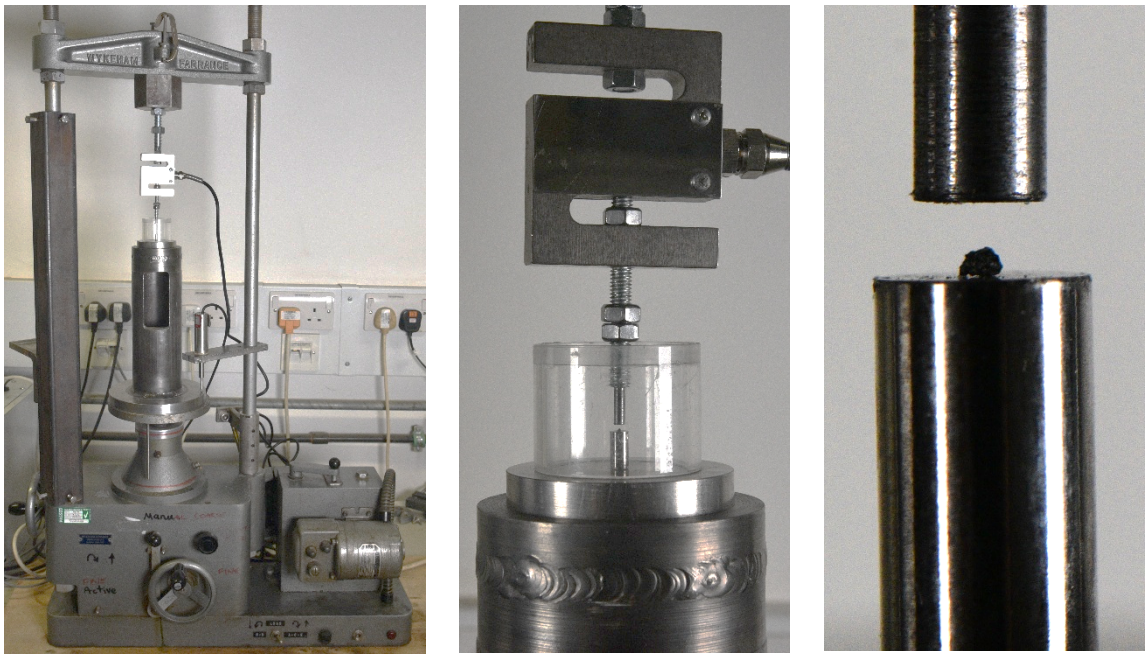

Figure 8. (left) Whole setup of loading frame, (middle) zoom in of load cell and platens, (right) particle in between the two platens.

A clear circular guard is also used once the particle is placed in the platens so that particles that fly away during critical failure can be noted and the proper failure mode identified. Since the particles being tested are on average 0.4mm, the speed at which the particles are moved together must be slow so that data of the loading stage can be sufficiently captured. Using table 7, the gears and the gear position inside the apparatus was changed to produce a feed speed of 0.0008in/min or 20.32μm/min.

Table 7. Gear speeds of the uniaxial loading machine

Approximate Rate of feed				Inches/minute		
Driver		30	60	36	54	45
Driven		60	30	54	36	45
Gear Change Positions	A	0.015	0.060	0.020	0.045	0.030
	B	0.003	0.012	0.004	0.009	0.006
	C	0.0006	0.0024	0.0008	0.0018	0.0012
	D	0.00012	0.00048	0.00016	0.00036	0.00024
	E	0.000024	0.000096	0.000032	0.000072	0.000048

3.3.1 Compliance test

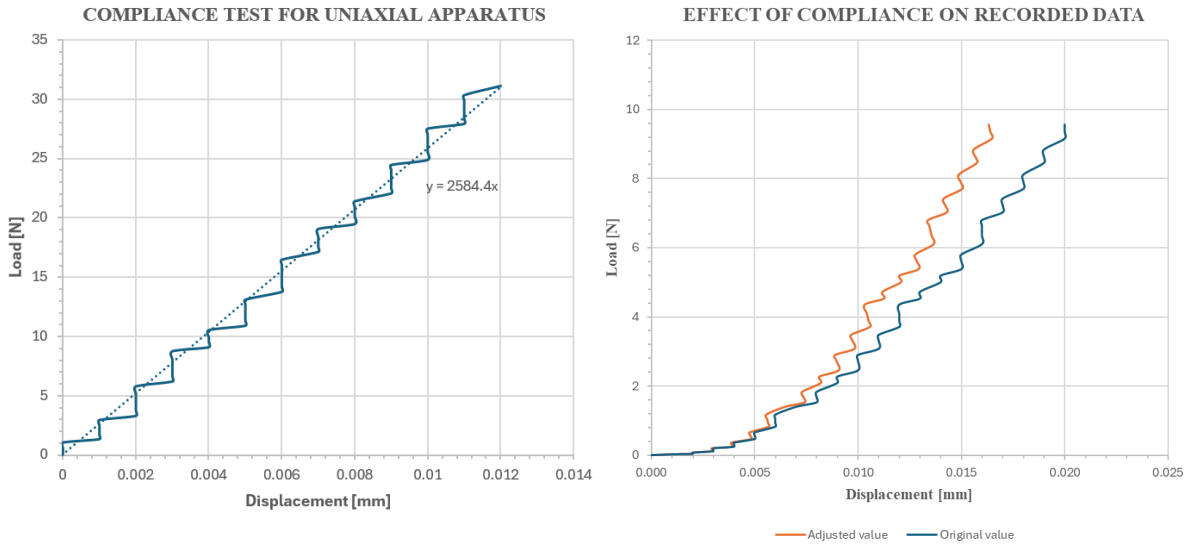

Figure 9. (Left) Compliance graph used to calculate gradient adjustment factor, (Right) Example of effect of compliance on basalt

In order to account for the stiffness of the loading system, a compliance test was carried out to quantify the deformation of the platens themselves. Since the platens possess their own flexibility, they deform slightly under load, meaning that the displacement recorded by the uniaxial load apparatus would otherwise overestimate the true particle displacement. To mitigate this effect, the platens were brought into direct contact without a particle between them and then loaded against each other. The resulting displacement was measured and plotted against measured load, with the gradient used to adjust the experimental data to provide corrected values for particle deformation under uniaxial loading (see figure 9).

3.2 Morphologi particle scanner

The Morphologi machine (see figure 10) is used to characterise the particle shape parameters outlined in section 2.4.1 with 5 magnification levels form 2.5x to 50x (see table 8).

Figure 10. Malvern Morphologi machine, equipped with 5 magnification levels and scans particles down to 0.5 microns (Malvern,2021)

It employs a dry powder dispersion method through the Sample Dispersion Unit (SDU), where a small amount of sample is placed and dispersed onto a glass plate using a controlled burst of compressed air. The SDU ensures particles are spread evenly and prevents agglomeration, allowing the instrument to capture accurate images of individual particles for reliable size and shape analysis. The machine is also encased within a clear tent to prevent dust infiltration onto the glass plate, with the plate cleaned between sessions to prevent cross contamination of samples.

After a simulant had been scanned multiple times, a filter was then included in the settings to exclude dust particles once the general characteristic values were known.

Table 8. Magnification level and particle size detection range on Malvern Morphologi G3

Magnification	***Particle size range [µm]***
2.5x	13 - 1000
5x	6.5 - 420
10x	3.5 - 210
20x	1.8 - 100
50x	0.5 - 40

3.3 Keyence Microscope

The Keyence microscope (see figure 11) is a high resolution 3D laser scanning confocal microscope for surface characterisation and particle imaging. Unlike the Morphologi, it can capture colour images and 3D surface profiles using laser for topographical and dimensional data.

Figure 11. Keyence microscope VK-X1000 series (Keyence, 2025)

Unlike the Morphologi, the Keyence can only scan one particle/object at a time and the magnification power is lower, therefore only larger fractions of the sample can be scanned. Minimal preparation is needed though; the particle only needs to be placed on the scanning platform and then brought into focus at the peak of the particle with the appropriate magnification.

The Keyence is particularly useful for identifying the constituent minerals in the simulants so that they can be separately tested and calculate their surface roughness (Sq). To do this, 5 different particles for each mineral were scanned and the average roughness calculated for use in the Hertz modelling.

Additionally the microscope was also used to determine the minimum and maximum feret diameters (d_1 and d_2) of the particles being crushed in the uniaxial loading frame from 3.1. These particles were crushed in the same order they were scanned in on the plate (see figure 12) with their surface topography and appearance also captured for further analysis.

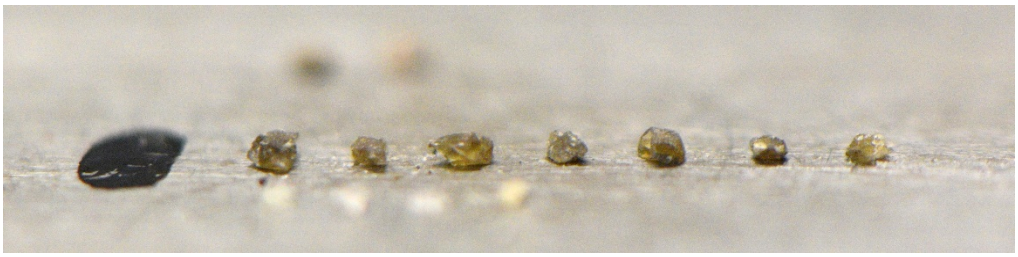

Figure 12. Pyroxene particles on a plate after scanning waiting to be crushed, the black line on the left indicates the side of the first particle

3.4 DSLR Camera

Since the Keyence microscope can only capture d_1 and d_2, a DSLR camera set up with LED uniform panel lights were used to capture d_3 as well as post crushing images of the particles to capture their fracture modes (see figure 13).

Additionally the DSLR camera was also used for general shots such as the simulant images in table 3.

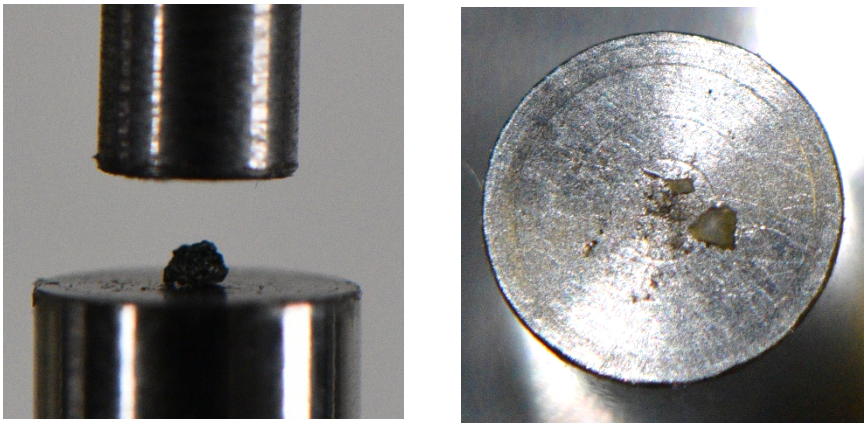

Figure 13. (Left) Front image of particle in between platens for d_3 measurement, top platen was used as scale with known diameter 3mm (Right) crushed sample of pyroxene

3.5 Interparticle apparatus

The last equipment used is the interparticle apparatus, seen in figure 14. Although developed to perform both normal and tangential loading, the horizontal actuators were malfunctioning and so only normal loading could be conducted on the simulants.

To perform the test, two particles are chosen, grinded on one side, and then glued to each platen (see figure 15). The peaks of the particles are then brought into contact and cyclic loading unloading is carried out.

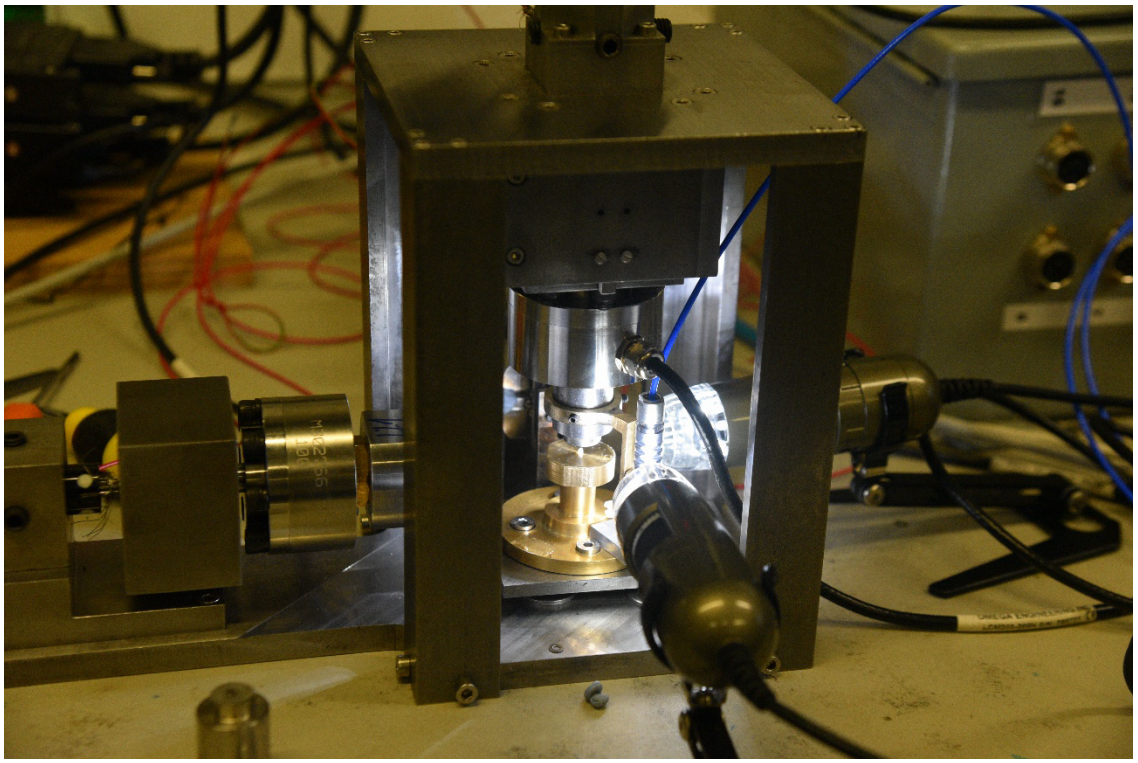

Figure 14. Interparticle apparatus with experiment in progress. Platens with the particles are situated in the middle of the frame with light and images provided by the microscopes either side.

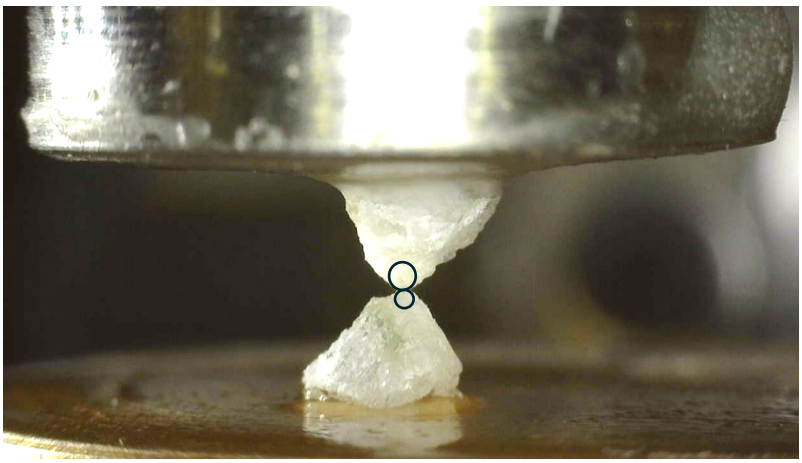

Figure 15. Image of two anorthosite particles with peaks in contact inside the Interparticle apparatus

4.KEYENCE MICROSCOPE

4.1 Basalt

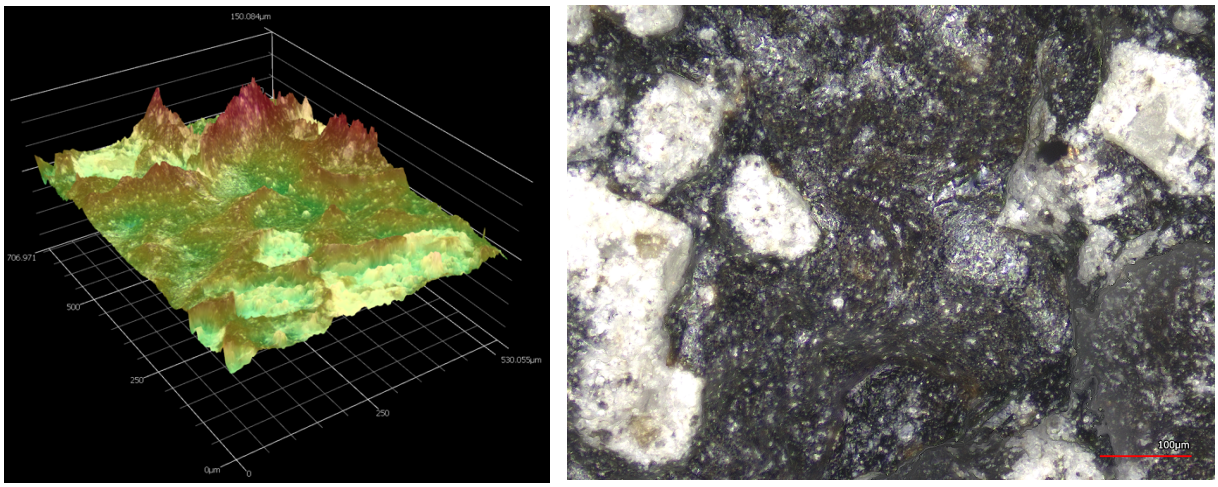

Figure 16. images of basalt. (Left) Surface corrected height map (Right) Optical image of particle at 20x

In Figure 16, the basalt particles are shown with a dark grey to black matrix containing lighter mineral inclusions. The particles are observed to range in size from fine grains to larger angular fragments. Their surfaces appear rough and irregular, with clear micro-topographic variation visible in the height map. The optical image shows crystalline inclusions embedded within the darker groundmass, indicating the heterogeneous composition and fractured surfaces typical of basalt.

4.2 Anorthosite

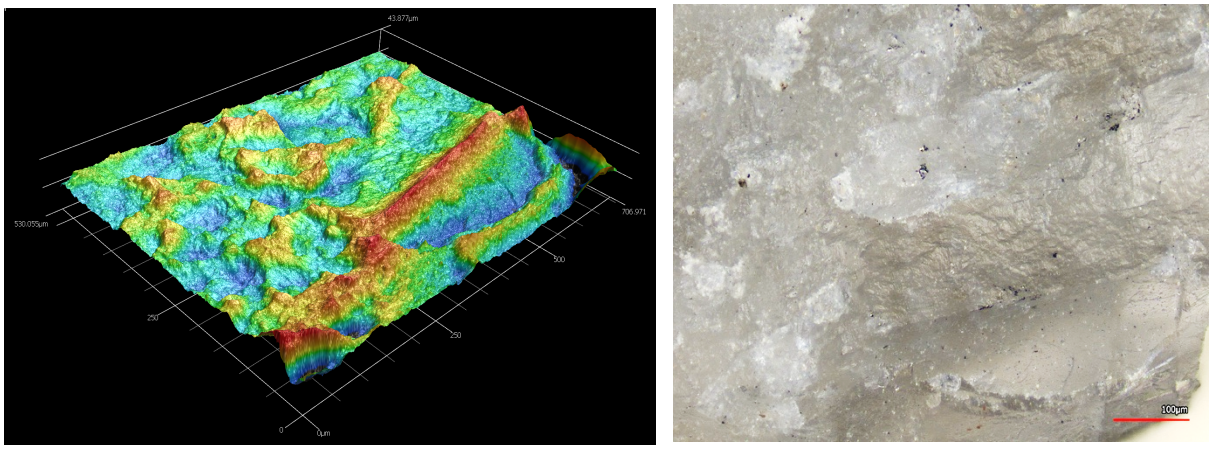

Figure 17. images of anorthosite. (Left) Surface corrected height map (Right) Optical image of particle at 20x

In Figure 17, the anorthosite particles are shown with a light grey to off-white colour and a relatively uniform appearance. Particle sizes vary but generally appear larger and less angular compared to the basalt. The surfaces are observed to be smoother overall, though the height map reveals distinct ridges and undulations. The optical image highlights a crystalline texture with fewer dark inclusions, indicating a more homogeneous composition characteristic of anorthosite.

4.3 Pyroxene

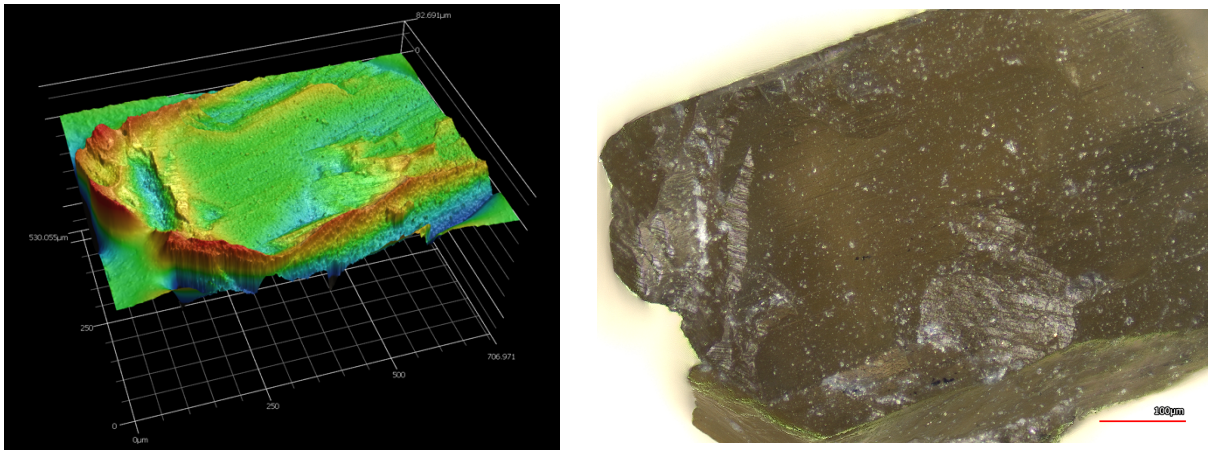

Figure 18. images of pyroxene (Left) Surface corrected height map (Right) Optical image of particle at 20x

In Figure 18, the pyroxene particles are shown with a dark brown to greenish colour and a glassy appearance. The particles are generally larger and display angular, blocky shapes with sharp edges. Surface features appear relatively smooth in some areas but with clear stepped fractures and uneven textures highlighted in the height map. The optical image shows a compact structure with subtle reflective surfaces, consistent with the crystalline nature of pyroxene.

4.4 Hostun

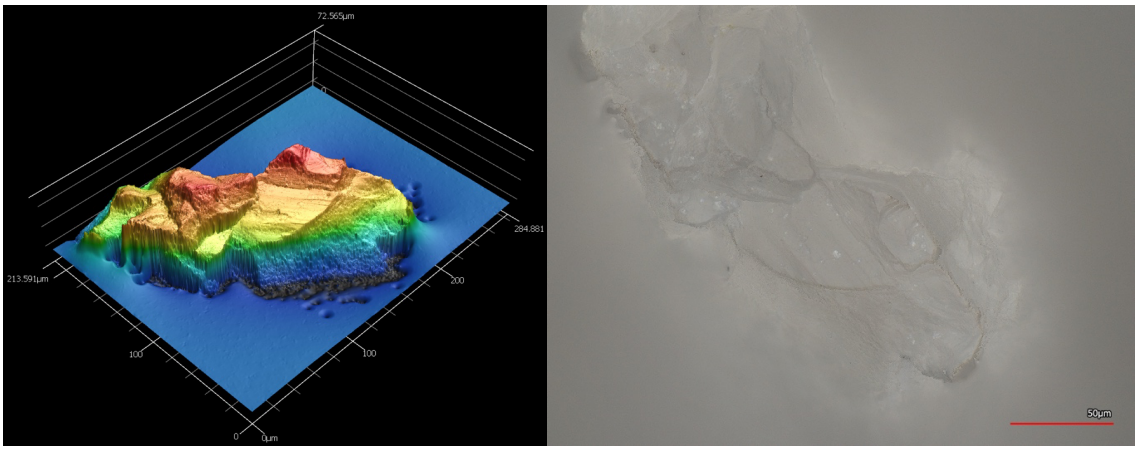

Figure 19. images of Hostun (Left) Surface corrected height map (Right) Optical image of particle at 20x

In Figure 19, the Hostun sand grains are shown with a light beige to off-white colour and a predominantly quartz composition. The particles are observed to be medium-sized, with diameters mostly between 0.1 mm and 1.0 mm. Their shapes appear sub-angular to angular, giving the grains a moderately rough surface texture. The distribution is relatively uniform, consistent with the poorly graded nature of Hostun sand.

5. UNIAXIAL LOAD CRUSH TEST RESULTS

Basalt, anorthosite, and pyroxene from the Exolith Lab simulants, together with Hostun sand composed primarily of quartz, were tested. For each mineral, 15 successful particle crushings were conducted, with spherical particles selected to maintain consistency with the modelling assumptions.

Particle RMS roughness was averaged over five measurements, while platen roughness was assumed equal for both sides as both were manufactured from a grinded E304 steel as only the upper platen was measured owing to the size of the lower platen being unable to fit in the scanner. Contact area was taken using the average radius over the 15 samples of a circle that circumscribes the arc of contact with the particle.

5.1 Basalt

For calculations, Youngs modulus and Poisson's ratio of Basalt were taken as 78Gpa and 0.25 (Schultz R.A., 1995) and for the platens as 190GPa and 0.265 respectively (AZO Materials,2019).

5.1.1 Load-displacement with Hertz modelling

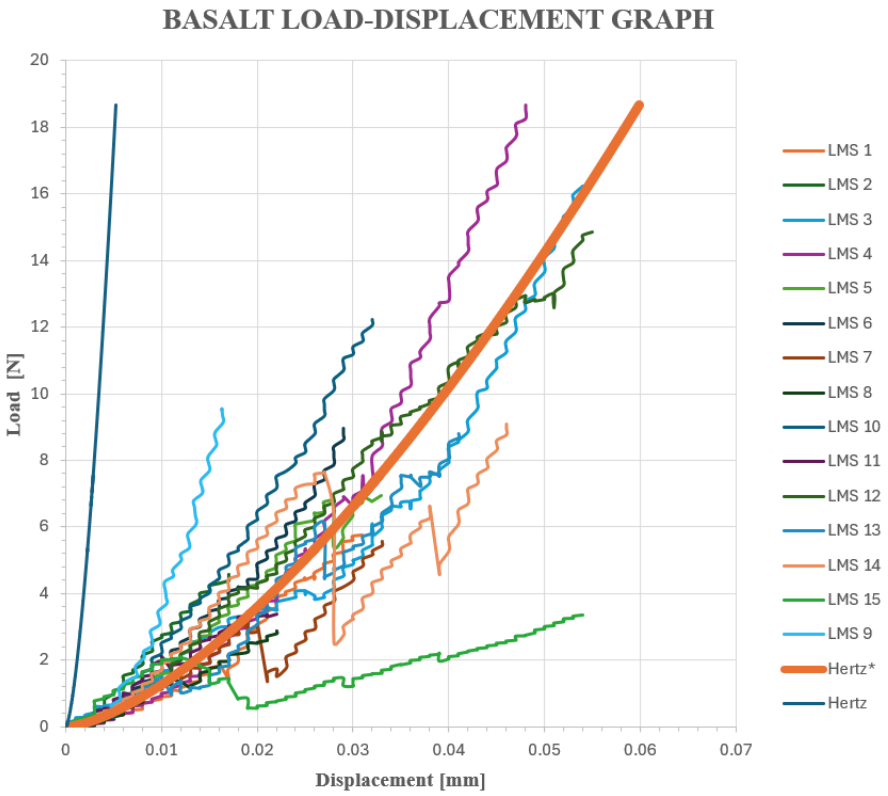

Figure 20. Load displacement graph for basalt from LMS sample with Hertz models

Table 8. Fracture mode for each basalt sample categorised using table 4

Sample	*1*	*2*	*3*	*4*	*5*	*6*	*7*	*8*	*9*	*10*	*11*	*12*	*13*	*14*	*15*
Type	*S*	*S*	*E*	*S*	*S*	*E*	*S*	*S*	*S*	*M*	*S*	*M*	*M*	*S*	*E*

Overall, significant scatter was observed, with many curves falling below the initial Hertz prediction. This discrepancy is likely due to the high RMS roughness of both particles and platens (12.32 µm and 4.84 µm respectively), which was accounted for in the modified Hertz* model, yielding a closer fit to the experimental data as shown by the thick orange line in Figure 20.

The variability in loading responses is also reflected in the distribution of fracture modes presented in Table 8. Particles sustaining the highest loads and strengths were generally of the explosive type, consistent with the findings of Wang and Coop (2016) and Figure 21. For basalt, however, explosive fractures comprised only 20% of cases, with splitting dominating at 60%, suggesting inherent planes of weakness associated with its amorphous structure. These fracture modes are illustrated in Figure 21 and 22.

5.1.2 Probability of Survival and Weibull modulus

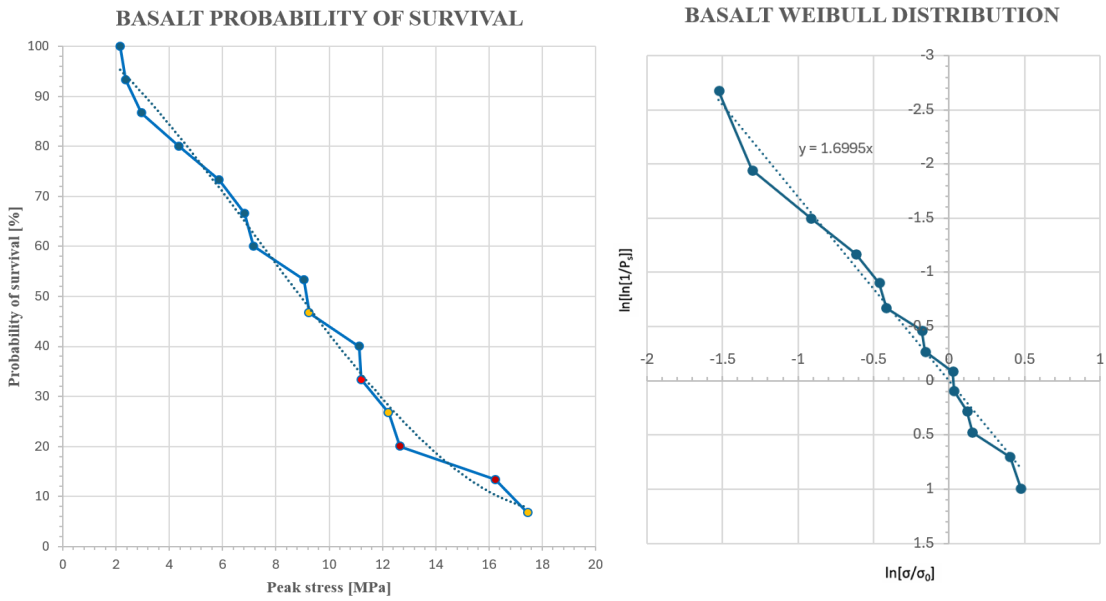

Figure 21. (Left)Probability of survival for Basalt. Blue indicates split fracture, yellow indicates mixed fracture, red indicated explosive fracture (Right) Weibull distribution

Figure 21 shows considerable variability in peak load and particle strength, with a characteristic strength of 10.85 MPa. The calculated Weibull modulus of 1.6995 is relatively low, indicating high strength variability and limited failure predictability, though it is comparable to the value of ~1.5 reported for completely decomposed granite (Wand and Coop, 2016)

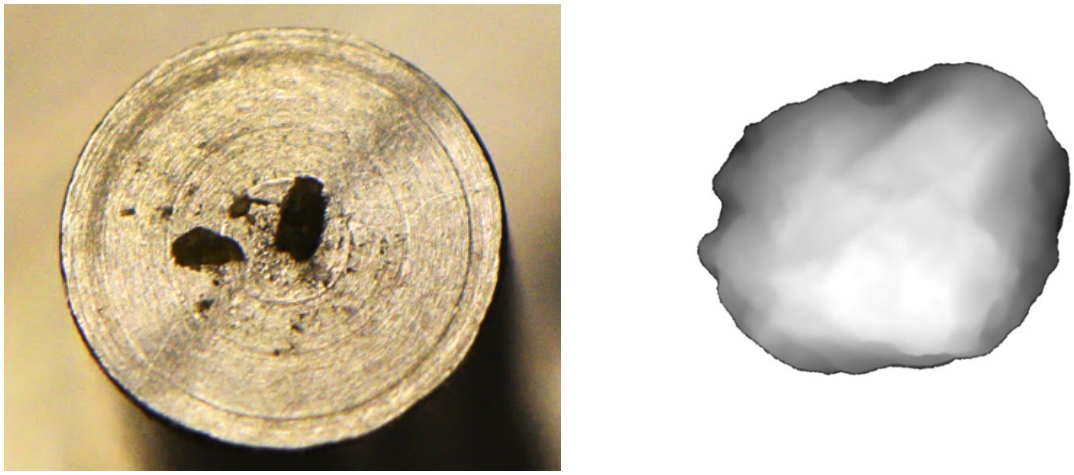

Figure 22. Image of a basalt particle after crushing. The particle has split into two main pieces with a third smaller one.

5.2 Anorthosite

For calculations, Youngs modulus and Poisson's ratio of Anorthosite were taken as 100Gpa and 0.27 (Ahrens A,2022). Since the platen remained unchanged, the values remain the same as section 4.1.

5.2.1 Load-displacement with Hertz modelling

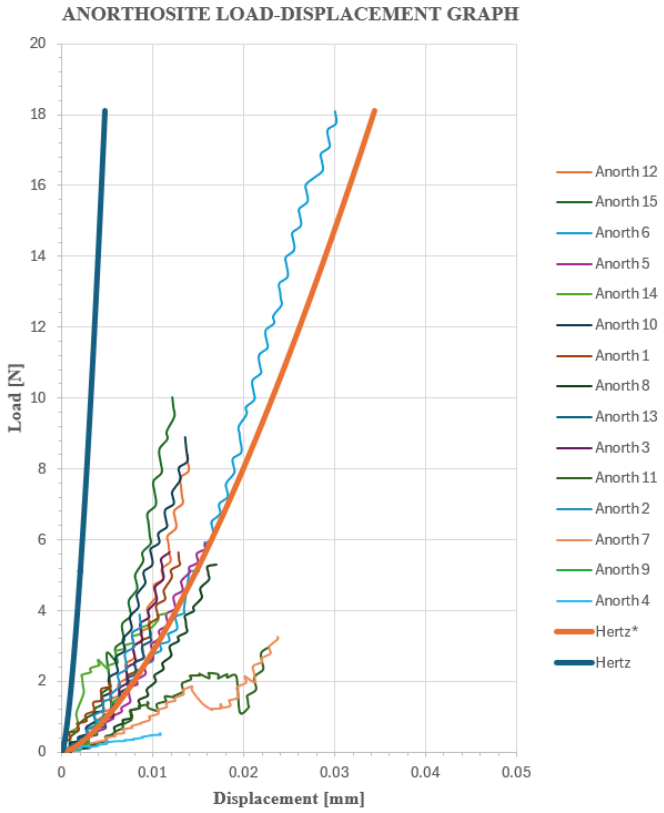

Figure 23. Load displacement graph for Anorthosite from LMS sample with Hertz models

Table 9. Fracture mode for each anorthosite sample categorised using table 4

Sample	*1*	*2*	*3*	*4*	*5*	*6*	*7*	*8*	*9*	*10*	*11*	*12*	*13*	*14*	*15*
Type	*S*	*S*	*S*	*S*	*M*	*E*	*S*	*S*	*M*	*S*	*S*	*M*	*M*	*S*	*S*

Similar to Basalt, the initial Hertz model in figure 19 over predicts the stiffness of the particles and is fitted much better by the Hertz* model including the platen roughness (as from 4.1) and the Anorthosite roughness of 7.91 µm. Additionally, the displacements induced by the loading are noticeably lower than that of the basalt which break around 0.035mm compared to 0.012mm for Anorthosite, indicating the anorthosite is more brittle than the basalt.

The anorthosite also leans towards a higher likelihood of splitting at 67% compared to 60% for basalt with the other 40% comprising of mixed mode for all but 1. The Anorthosites ability to reach higher loads in smaller displacements contributes to its slightly higher characteristic strength of 17.46MPa, derived from figure 24.

5.2.2 Probability of survival and Weibull modulus

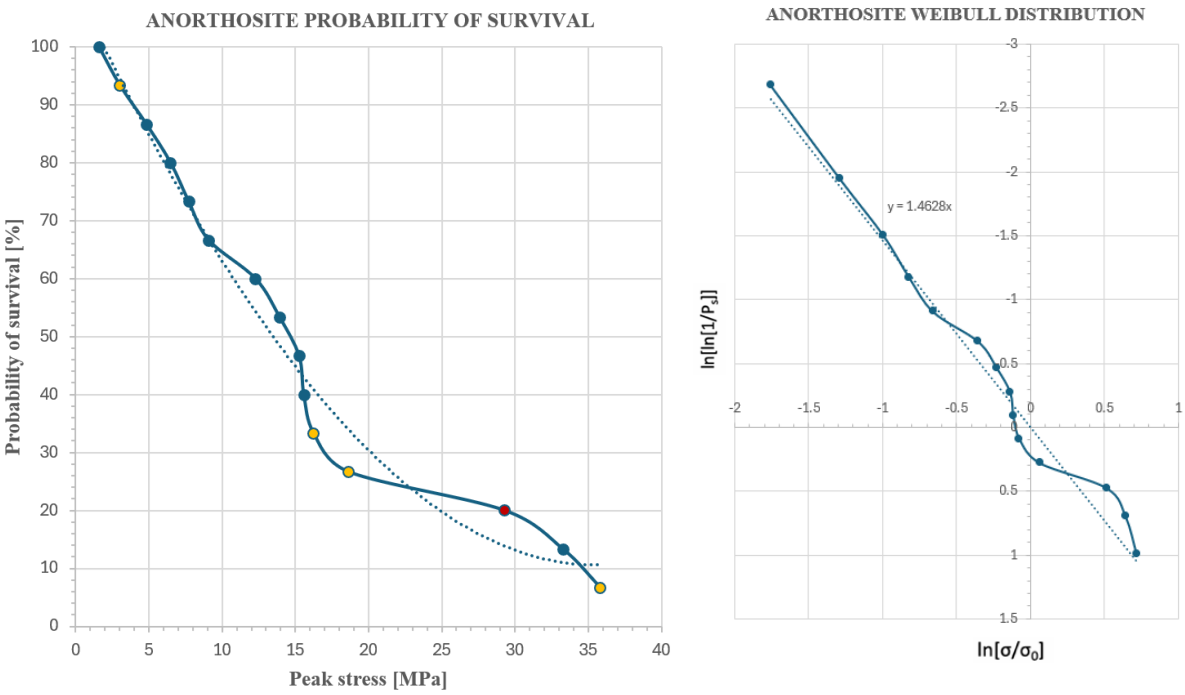

Figure 24. (Left)Probability of survival for anorthosite. Blue indicates split fracture, yellow indicates mixed fracture, red indicates explosive fracture (Right) Weibull distribution

Using figure 24 (Right), the Weibull modulus for Anorthosite was calculated as 1.4628, slightly lower than that of Basalt indicating it exhibits a greater variation in strength. The gaps between points within the probability of survival graph are also more varied for Anorthosite, particularly at the higher stress levels. This could be due to the smaller than average size of the top three peak stress particles, which could be a factor in their higher strengths (McDowell and Bolton,1998).

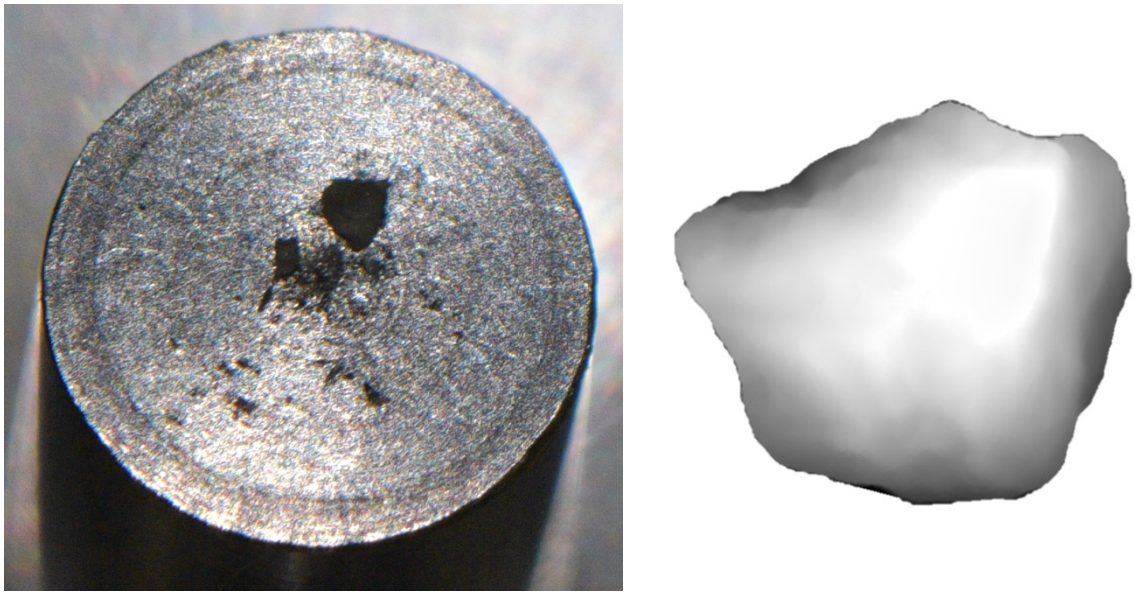

Figure 25. Image of a anorthosite particle after crushing. The fracture mode was classified as mixed due to the presence of both larger particles and finer powder present

5.3 Pyroxene

For calculations, Youngs modulus and Poisson's ratio of Anorthosite were taken as 186Gpa and 0.21 (Jackson et al ,1999). Since the platen remained unchanged, the values remain the same as section 4.1.

5.3.1 Load displacement graph with Hertz modelling

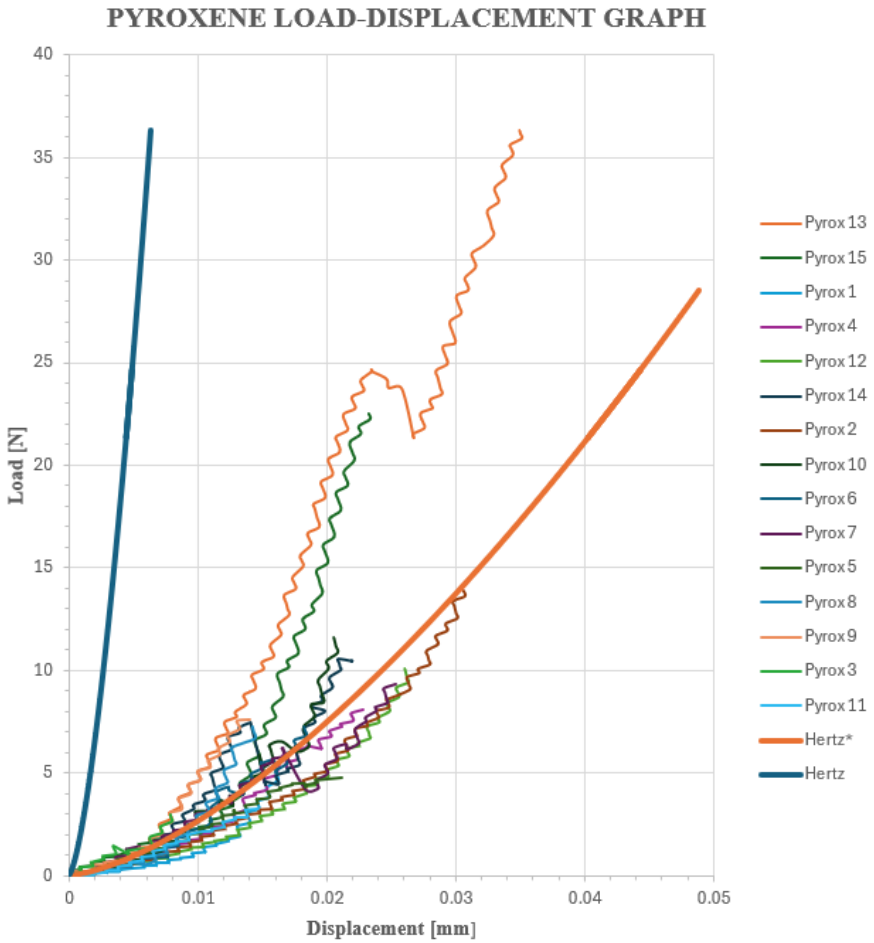

Figure 26. Load displacement graph for pyroxene from LMS sample with Hertz models

Table 10. Fracture mode for each pyroxene sample categorised using table 4

Sample	*1*	*2*	*3*	*4*	*5*	*6*	*7*	*8*	*9*	*10*	*11*	*12*	*13*	*14*	*15*
Type	*S*	*E*	*E*	*S*	*S*	*M*	*M*	*S*	*S*	*M*	*S*	*S*	*E*	*S*	*E*

Again as with the previous minerals, the initial Hertz model in figure 26 over predicts the stiffness of the particles and is fitted much better by the Hertz* model which includes the platen roughness (as from 4.1) and the pyroxene roughness of 14.08 µm; the highest of the minerals so far. Additionally, the displacements induced by the loading seem to average slightly higher than the anorthosite and slightly lower than the basalt, but peaks at around the same load for a slightly larger than average particle size compared to the other two.

The fracture mode is also more varied with a mixture of split, explode and mixed compared to the previous two.

5.3.2 Probability of survival and Weibull modulus

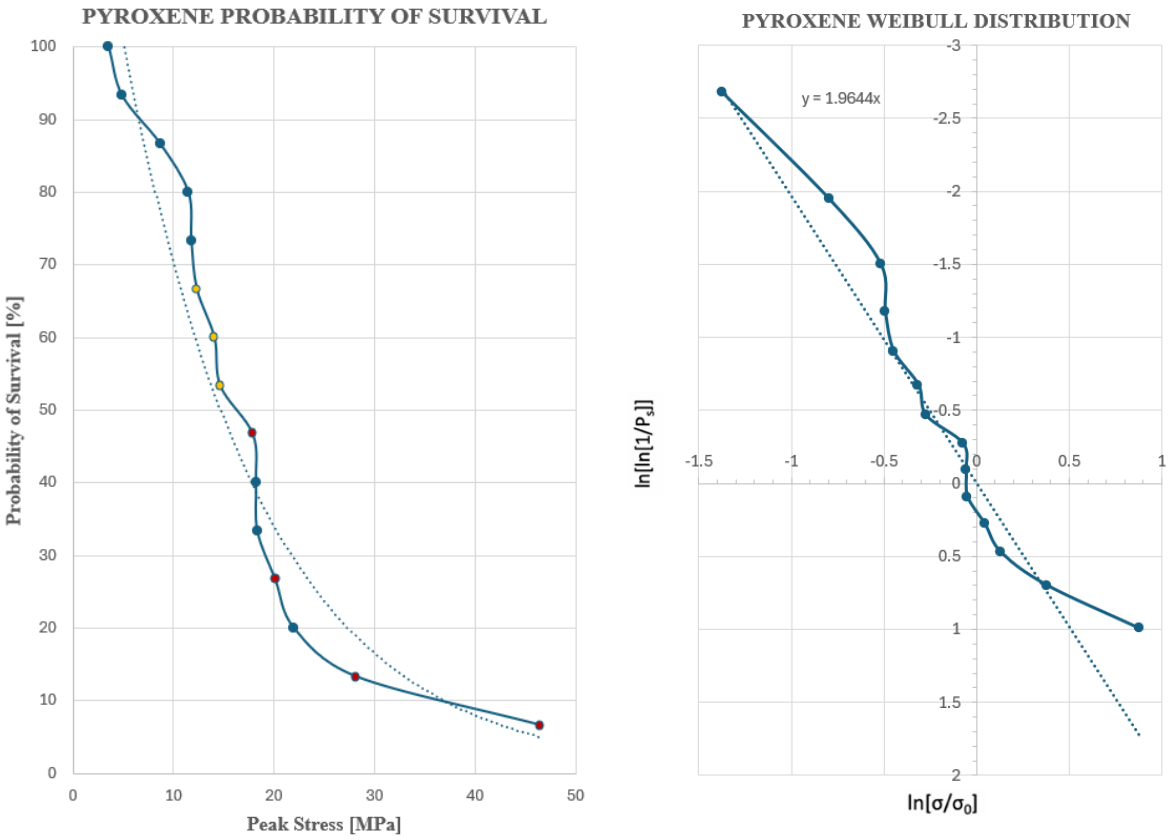

Figure 27. (Left)Probability of survival for pyroxene. Blue indicates split fracture, yellow indicates mixed fracture, red indicates explosive fracture (Right) Weibull distribution

Using figure 27 (Right), the Weibull modulus for Pyroxene was calculated as 1.9644, the highest of all the minerals. This slightly increases the predictability of its failure, which is particularly useful for the Mare simulant categories, made up of around 25-35% Pyroxene according to table 1 and 2. Additionally looking at figure 27 (left), the explosive particles generally withstand the highest loads as expected.

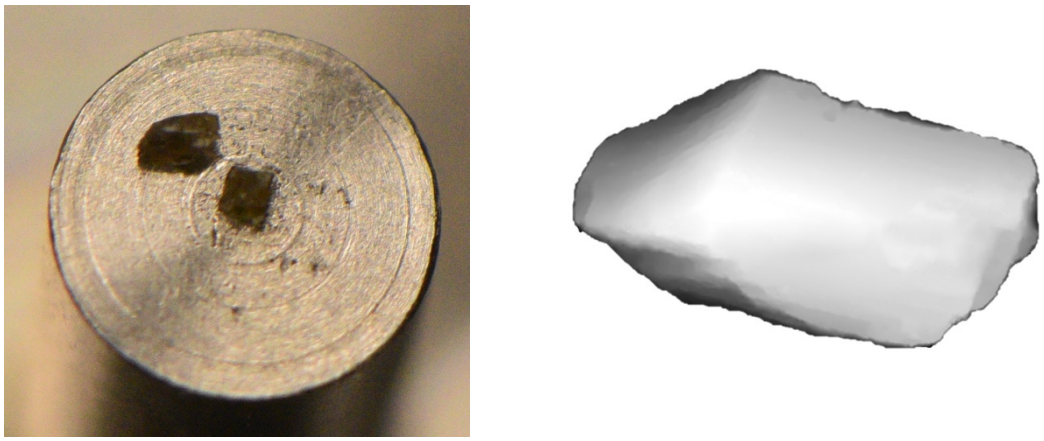

Figure 28. Image of a pyroxene particle after crushing. The fracture mode was classified as split due to the presence of two large fractions of the original particle with no other components

5.4 Quartz (Hostun sand)

For calculations, Youngs modulus and Poisson's ratio of Anorthosite were taken as 96Gpa and 0.0665 (Coop M, 2024). Since the platen remained unchanged, the values remain the same as section 4.1.

5.4.1 Load displacement graph with Hertz modelling

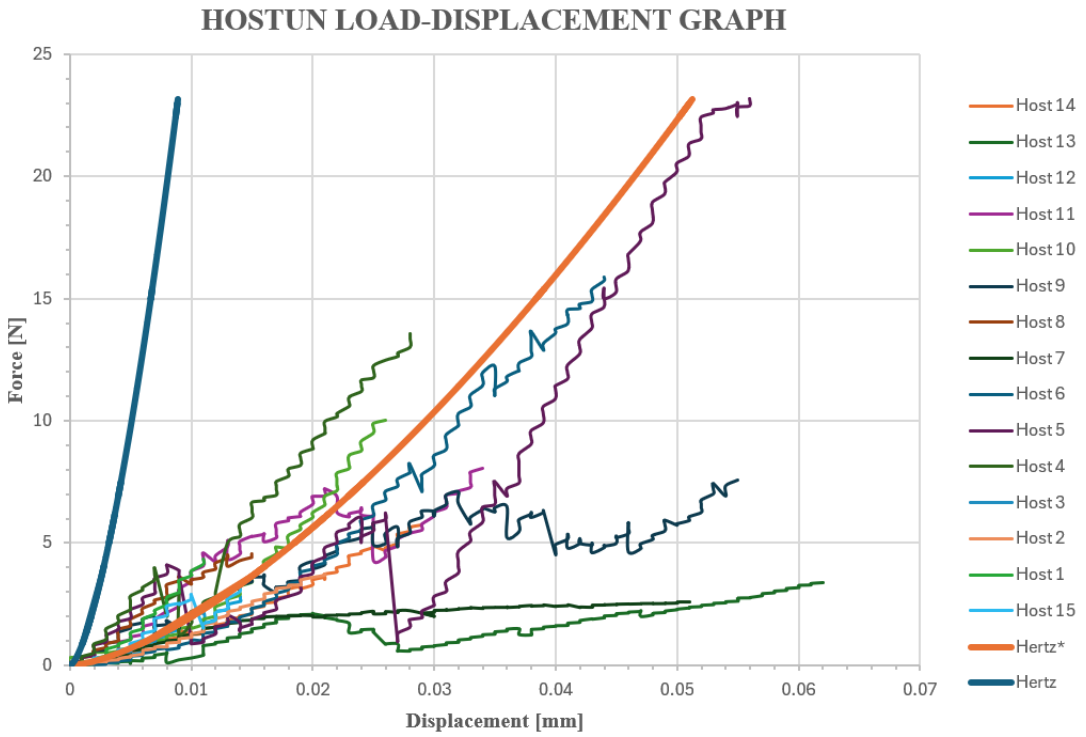

Figure 29. Load displacement graph for pyroxene from LMS sample with Hertz models

Table 11. Fracture mode for each Hostun sample categorised using table 4

Sample	*1*	*2*	*3*	*4*	*5*	*6*	*7*	*8*	*9*	*10*	*11*	*12*	*13*	*14*	*15*
Type	*E*	*CR*	*CR*	*E*	*E*	*CR*	*S*	*CR*	*CR*	*E*	*E*	*E*	*S*	*E*	*CR*

Similar again to the earlier minerals, the first Hertz model over predicts the stiffness of the particles by a visible difference but is much better fitted by the Hertz* model with Hostun averaging a roughness of 3.214µm. Even though this is the lowest roughness recorded of all the minerals and the platen, the fact there is still a clear difference between Hertz and Hertz* reinforces the need for the inclusion of roughness in Hertz calculations to be able to make substantial ally better predictions.

Interestingly, the fracture mode of the Hostun sand compared to those from the Exolith simulant is also noticeably different. The quartz appears to have a preference towards the explosive and core remaining type, seen in table 11. This behaviour is expected of a quartz sand, as explored by Wang and Coop, 2016. This more non linear fracture type can also be seen in the loading lines in figure 29 which fluctuate more due to chipping and residual cores varying the load, compared to the relatively smooth lines of the Exolith simulant minerals.

Another factor that made it slightly harder to determine the true fracture point of the particles was the smaller sized particles (around 0.2mm diameter) compared to the Exolith minerals which could be seen better with the naked eye. In future a high-speed camera or microscope could be set up such as in Wang

and Coop 2016 to better distinguish between chipping, asperities or explosive fractures that then remain on the platen taking load without a clean drop to 0N.

5.4.2 Probability of survival and Weibull modulus

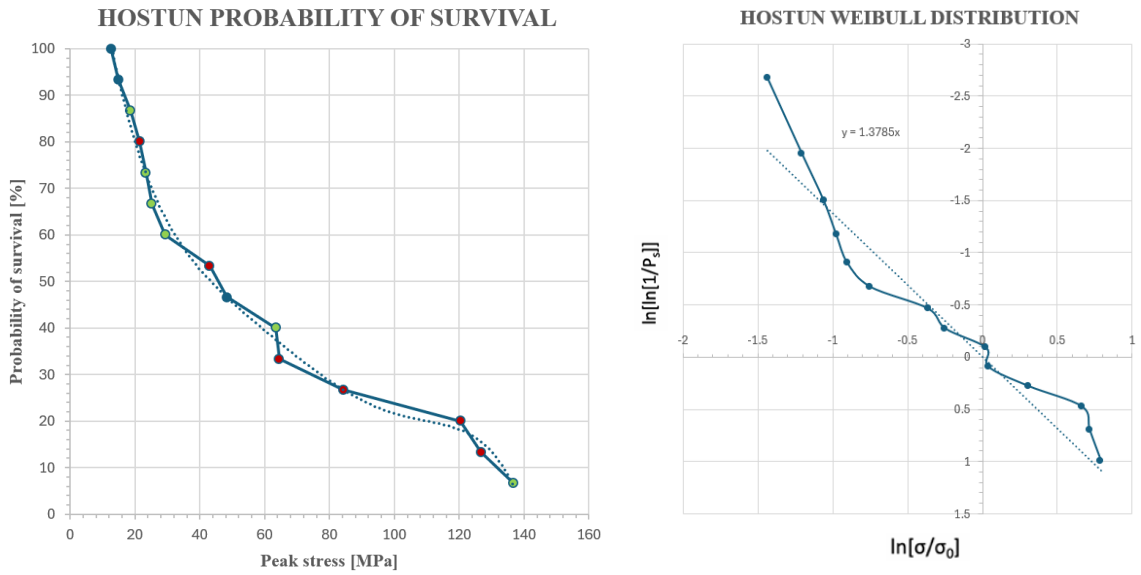

Figure 30. (Left)Probability of survival for Hostun. Blue indicates split fracture, green indicates core remaining fracture, red indicates explosive fracture (Right) Weibull distribution

Finally, the characteristic strength of Hostun was found to be significantly higher than that of the Exolith simulant constituents, reaching 62 MPa. The Weibull modulus was calculated as 1.3785, indicating that Hostun exhibited the greatest variability in peak stress behaviour among the tested materials. This highlights a marked difference in mechanical response between Hostun and the Exolith simulants, causing them to behave distinctly under applied loads. Hostun is therefore more likely to withstand higher loads; however, it subsequently fractures more violently, with a greater impact on long-term creep and settlement. The finer particles are redistributed into voids, resulting in unpredictable areas of consolidation.

5.5 Comparisons and conclusions

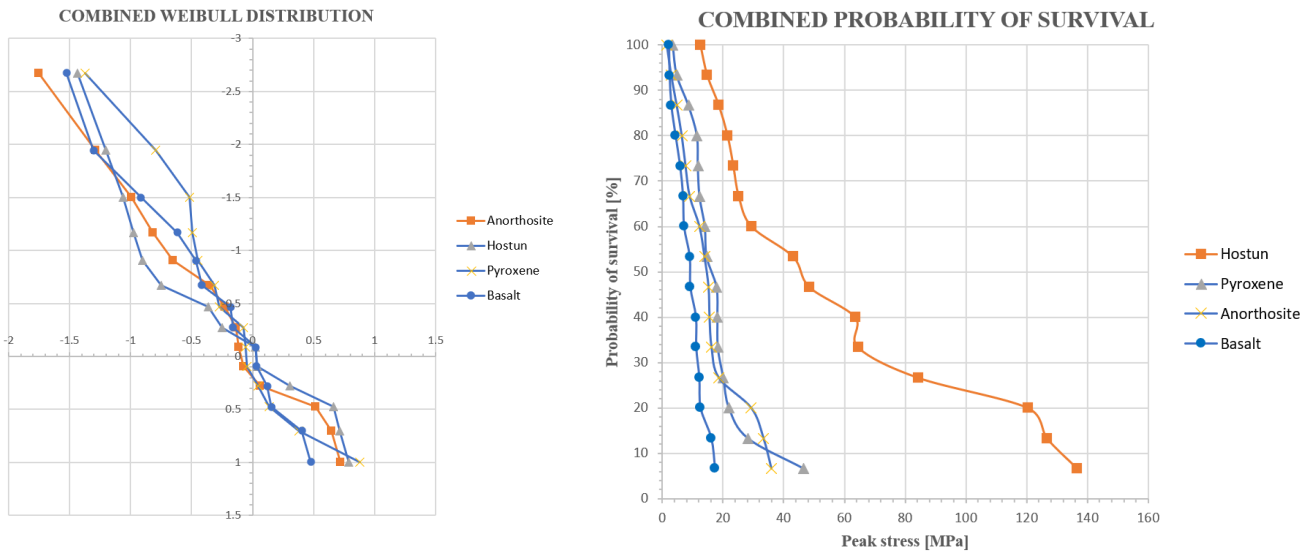

Figure 31. Combined simulant graphs for probability of survival (Left) and Weibull moduli (Right)

As no Weibull parameters exist for actual lunar regolith, experimental data parameters can therefore carry uncertainty when trying to determine its similarity to real lunar regolith behaviour, particularly regarding fracture mode, its effect on fines production and the load bearing capacity. This has direct implications for lunar mission planning: shattering of weak grains could increase dust hazards, reduce bearing capacity, and accelerate settlement under landers or habitats, affecting mobility, surface operations, and long-term infrastructure stability.

Exolith simulants with their accurate mineralogy and closer replicated particle sizes would therefore be assumed to act the closest to that of real regolith since Weibull moduli and characteristic strength are properties influenced by mineralogy and internal structure which are better replicated by the samples with the closest mineralogy. Therefore in cases where the load bearing capacity and fracture mode are being considered, such as for testing foundations, Hostun would be inappropriate to use due to its significantly higher Characteristic strength (as seen in figure 31 right), differing fracture mode and higher unpredictability due to a lower Weibull modulus.

6.MORPHOLOGI TESTS

For each simulant type, the same sample was scanned at 10x and 20x for continuity so that the levels of magnification could be compared to determine repeatability of particle characteristics and accuracy. At these magnifications, particles from 1.8 microns to 210 microns can be appropriately captured (see table 8).

Due to the fine nature of the samples being studied, it was found that a sample size of $1mm^3$ (equivalent to about 900,000 particles) was the maximum volume the machine could study without crashing, with $0.5mm^3$ was found to be more optimal.

After testing it was determined that the 10x magnification was not powerful enough and was producing too many particles with a pixel size lower than the threshold mentioned in section 2.4.3 (also see table 12) Therefore, the graphs produced at 10x were not appropriate, see figure 32 for an example. Ideally 50x would have also been scanned but the lens was malfunctioning and therefore could not be carried out.

Table 12. Minimum criteria for ensuring reliable particle shape characterisation in pixels (Q Sun et al, 2019)

Shape descriptors		L_{min}	P_{min}	Sqrt(A)$_{min}$	Hierarchy
Aspect ratio (AR)		25	100	25	**Coarse descriptors**
Circle ratio sphericity (S_C)					Evaluating principal dimensions of particles
Diameter sphericity (S_D)		100	350	75	**Medium coarse descriptor**
Area sphericity (S_A)					Related to areas of particles
Perimeter sphericity (S_P)		130	400	100	**Fine descriptor**
Circularity					Related to perimeter of particles
Convexity		250	900	200	**Very fine descriptors**
Roundness (R)	Very angular to angular ($0 < R < 0.17$)				Evaluating perimeters of particles
	Angular to rounded ($0.17 < R < 0.70$)	130	550	100	
	Rounded to well-rounded ($0.70 < R < 1.0$)	75	350	70	

Additionally, Hostun was scanned at 10x, however failed to scan at 20x for unknown reasons many times so unfortunately will not be included in the Morphologi tests at 20x.

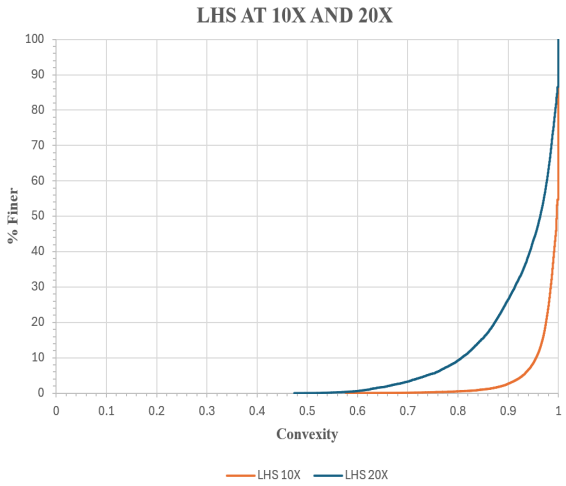

Figure 32. Comparison of LHS for convexity. A clear difference between 10x and 20x can be seen, with 20x better replicating the expected curve shape

6.1 Particle shape and surface characteristics

Below in figure 33, 4 of the main particle surface characteristics can be seen. Noticeably, the characteristics with lower pixel thresholds produced better quality graphs as expected. Further to this, a limitation of the 20x magnification has been identified for the CE diameter graph which normally tails off at the end however in the case of the 20x magnification, abruptly stops. This doesn't necessarily impact the validity of the graph only the validity potentially at the tail end. This region would be further clarified at 50x.

- **CE diameter:** distributions of the different simulants produce similar results with only minor differences above the 50% finer section for Highland and South pole, indicating a predicted general consistency in particle size across the lunar surface.
- **Circularity:** More visible variance by sample. LMS and LHS follow each other closely whilst LSP predicts the highest average circularity. Regolith appears in order of Anorthosite content, implying therefore the higher the Anorthosite content the lower the circularity.
- **Aspect ratio:** Samples more closely follow each other, particularly above values of 0.8 and above, making up 65% of the sample. Only minor divergence seen by LMS below 35% finer indicating general particle consistency in aspect ratio.
- **Convexity:** similarly to circularity some variance is seen but samples follow the same pattern, with LMS and LHS following closely and LSP predicting the highest average convexity. This could therefore imply the more anorthosite rich the sample, the more convex the particles since LSP is 90% anorthosite.

-

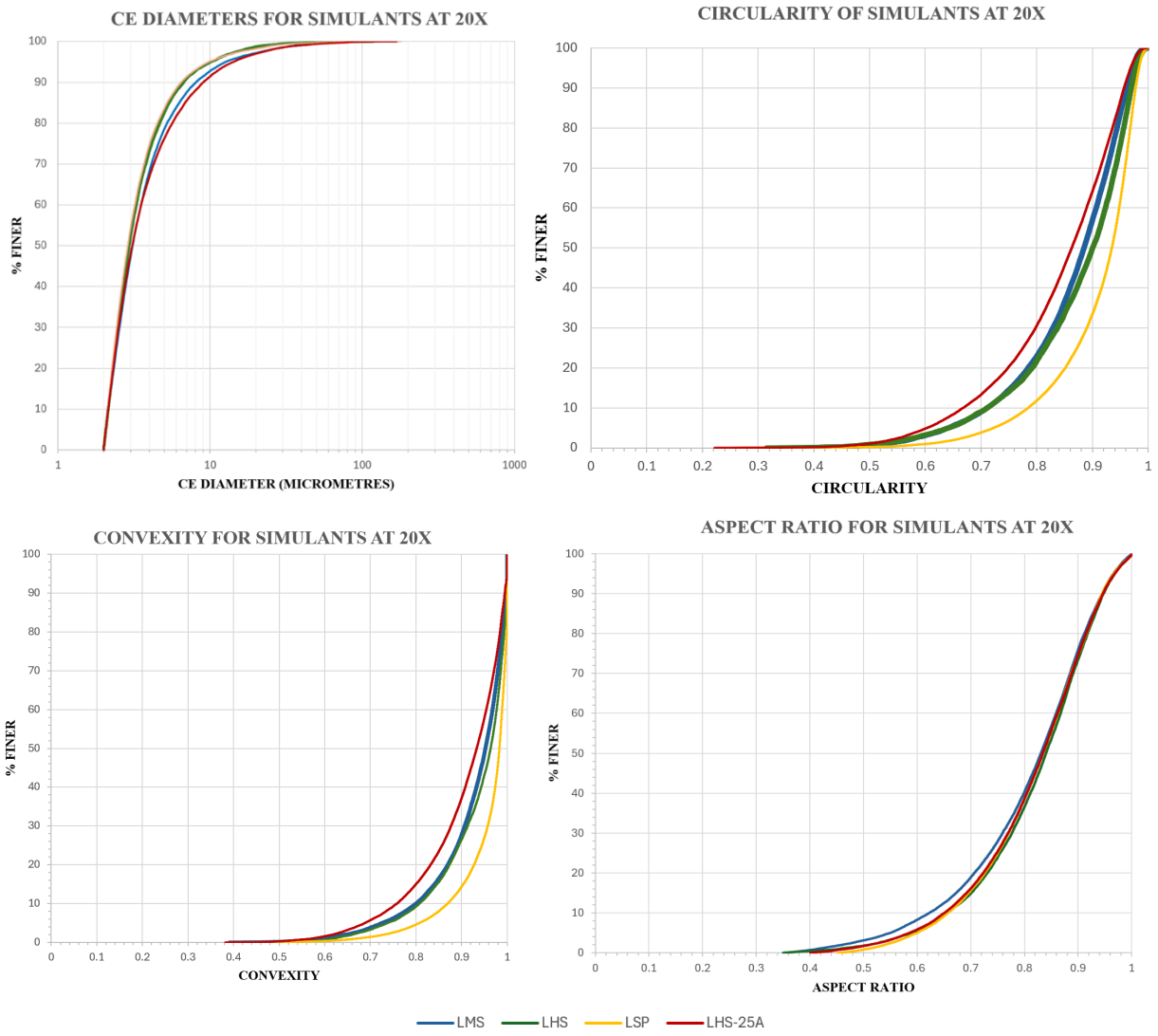

Figure 33. Particle characteristic graphs for regolith samples LMS,LHS,LSP etc using Morphologi

6.1.1 CE diameter

Comparisons can now be made between my data and the data outlined from the NASA Simulants guide A that is available. As of current no data on convexity or circularity is available, and analysis has only been conducted on LMS-1 and LHS-1.

Table 13. CE Diameter comparison of simulant and Apollo retrieved samples for Mare and Highland in micrometers

Sample	*Simulant*			*Real regolith*		
quartile	*Q25*	*Q50*	*Q75*	*Q25*	*Q50*	*Q75*
LMS	*2.43*	*3.09*	*4.58*	*24.4*	*65.1*	*182.1*
LHS	*2.38*	*2.94*	*4.14*	*24.1*	*118.1*	*386.2*
LSP	*2.35*	*2.88*	*4.01*	*N/A*	*N/A*	*N/A*
LHS-25A	*2.4*	*3.08*	*4.82*	*N/A*	*N/A*	*N/A*

The simulants are significantly finer than the real regolith samples. This would partly be due to the manufacturing size limit of the regoliths of 2000 which automatically eliminates the upper fractions from being replicated, but could also be due to the dispersion method. Although larger sample volumes were preferred, due to the large percentage of fines a volume of only 1mm cubed produced over a million particles and crashed the software therefore the smaller samples volume used may have skewed the distribution to the finer end. Other studies conducted on LMS and LHS produced quartiles in a similar range to the real regolith such as SDL 2022, however their method is not explained in detail in the NASA simulant guide and so the accuracy of the instruments cannot be assessed, with the data I collected suggesting much finer samples than expected across the board.

6.1.2 Aspect ratio

Regarding aspect ratio, only a bulk property is available from the NASA simulant guide for the Apollo samples measured using a MicroTrac SYNC Particle Size and Shape Analyser and averaged over the different samples.

Table 14. Aspect ratio of simulants compared to real lunar regolith

Sample	***Simulant***	***Real regolith***
LMS	*0.80*	*0.70*
LHS	*0.82*	
LSP	*0.82*	
LHS-25A	*0.81*	

Values for the simulants are slightly higher than that of the real regolith, implying that the simulants are more circular in shape. This is to be expected though, as minerals collected from the Earth will experience many kinds of weathering which will tumble and transform them into more spherical particles, compared to the lunar regolith which only weathers through asteroid impact which has little effect on rounding.

6.2 Roundness analysis

Table 15. Roundness values for simulants by region

Sample	***Value [nd]***
LMS	*0.59*
LHS	*0.61*
LSP	*0.56*
LHS-25A	*0.59*
Hostun	*0.68*

Table 16. Roundness values for simulants by mineral

Sample	***Value [nd]***
Basalt	*0.69*
Anorthosite	*0.59*
Pyroxene	*0.59*
Quartz	*0.68*

The roundness analysis shows variation in simulants when grouped by region and mineral. Regionally, values range from 0.56 (LSP) to 0.68 (Hostun), with most lunar simulants lying between 0.59 and 0.61. By mineral, basalt and quartz display higher roundness (0.69 and 0.68), while anorthosite and pyroxene are less rounded (0.59). These differences are significant for geotechnical

behaviour, as particle shape influences density, shear strength, and flow properties. More rounded particles compact more easily but provide less interlocking, which may reduce shear resistance. Less rounded particles interlock more effectively, improving strength but making excavation and handling more difficult. This highlights the importance of accounting for particle morphology when selecting simulants for construction-related testing.

7.INTERPARTICLE TESTS

7.1 Normal loading

Since the particles can only withstand low forces due to their size, the maximum force applied was 20N. Additionally due to the limitations of the apparatus, only the larger fractions of the simulants could be used (between 1-2mm in diameter) and so unfortunately Hostun could not be tested in the apparatus.

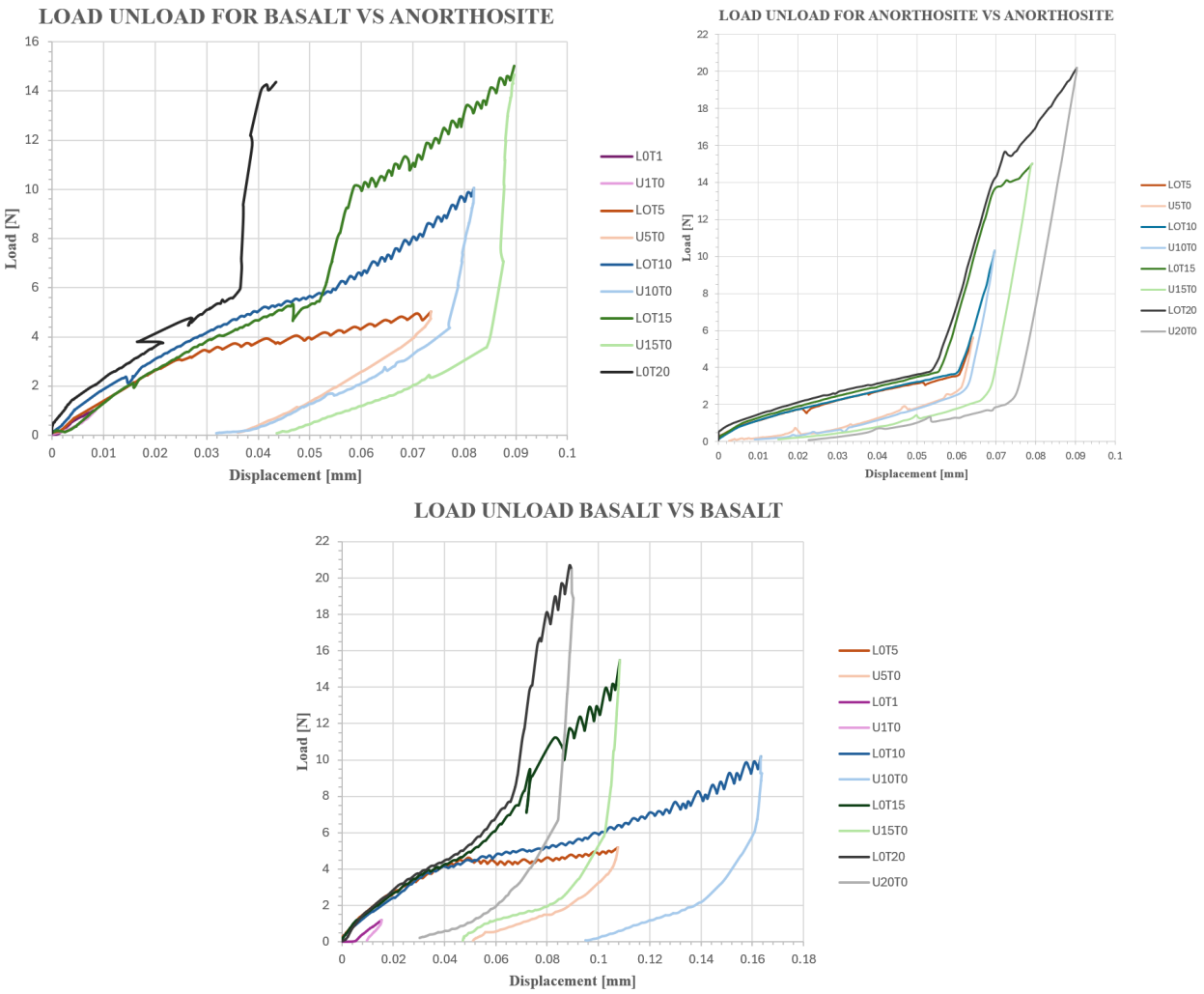

Figure 34. Cyclic loading inside interparticle testing machine, carried out in three mineral interactions

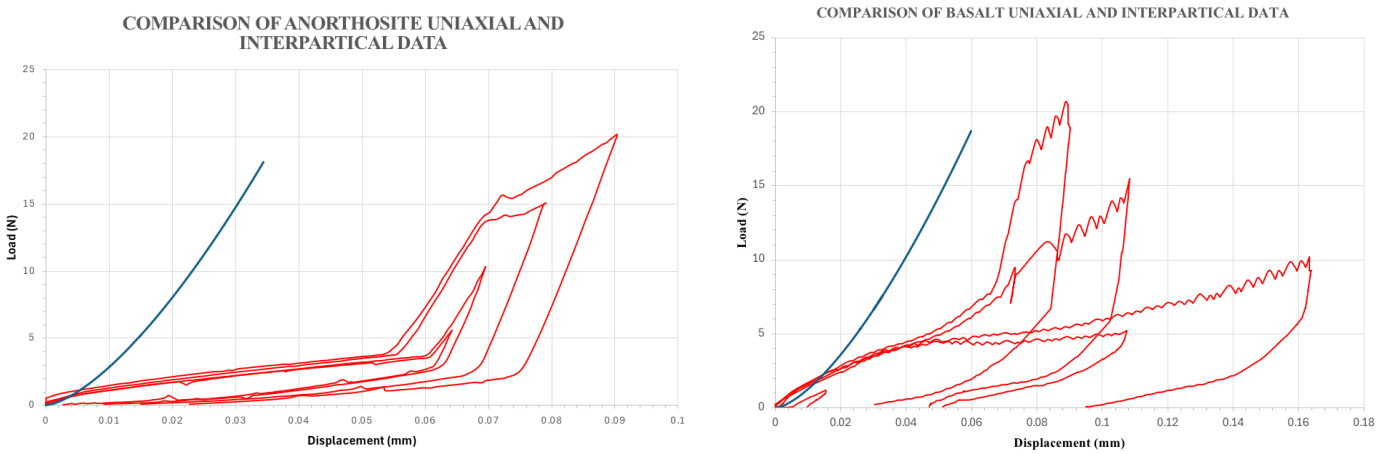

Figure 35. Comparison of interparticle and uniaxial particle interactions, lined in red indicate the cyclic loading

During interparticle testing, 3 types of contacting pairs were tested due to size requirement of the apparatus. From left to right clockwise in figure 34, Basalt vs Anorthosite (also seen in figure 36), Anorthosite vs Anorthosite and Basalt vs Basalt. Unfortunately, the tangential loading component was not operable at this stage and so only normal cyclic loading was carried out. For same mineral interactions (left and middle of figure 10), the hertz* graphs can also be plotted for comparison. Results vary quite vastly between uniaxial and interparticle, however the gradients of the predictions and the raw data do match during the elastic loading phase.

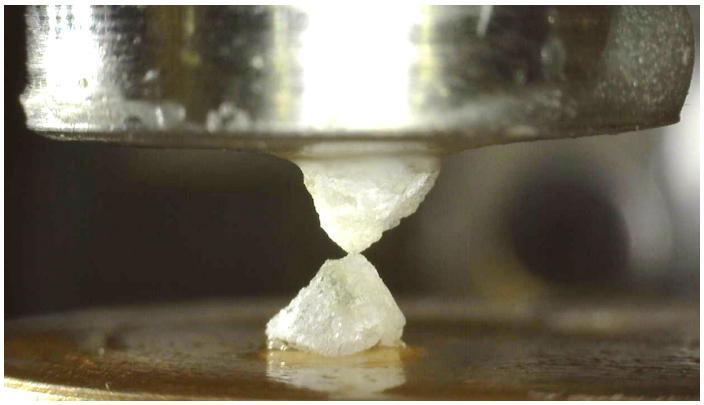

Figure 36. Image taken of Anorthosite vs Anorthosite inside the interparticle apparatus, particles used are around 1mm in diameter.

For the Anorthosite, there is some initial rather soft behaviour until 0.055mm range, followed by a distinct increase with gradient matching that of the prediction in blue. This initial softer behaviour may be caused not by distortion of the particles themselves but potentially poor adhesion/gluing which is emulating the sudden increase in displacement. The true loading therefore starts from about 4N, passing from a near elastic Hertz type response to a yield at about 14N. After which, there are elasto-plastic displacements so the unloading is on a parallel curve to the loading – the distance between the loading and unloading curves (after the initial flat response) is the plastic displacement. For this loading cycle, the particle crushing strength is at 20N so there is a large amount of strain hardening between yield and breakage, however further cycles at higher loads should be conducted to verify this.

For Basalt, a slightly different behaviour is observed. The high Sq surface roughness of the Basalt particles can be seen influencing the behaviour during loading, creating the slightly softer waved lines before the more typical elastic behaviour is observed around 5N. Similarly to the Anorthosite, a near elastic behaviour mimicking the prediction is observed until around 16N after which the line begins to tail and fluctuate, indicating plastic loading. The plastic deformation that has occurred during the unloading stages is evident by the non zero finishing displacement values. If all loading cycles were elastic, all lines would return to the origin.

8.CONCLUSIONS

In conclusion, preliminary results for the properties of the simulants have been defined, however further work is clear to further validate the results, such as the need for a 50x magnification for Morphologi data. Physical properties such as Weibull moduli have been defined for the main component minerals, allowing for initial modelling accuracy for applications such as DEM, however further testing should be conducted to raise the number of tests per mineral to 30 to test repeatability and patterns, as well as broaden the testing to Olivine and Ilmenite, in addition to other simulants. For the particle shape and surface characteristics, initial findings are promising and highlight potential need for updating existing data on the true regolith within the NASA guide. Although the interparticle testing was not as successful as hoped, it has allowed for some identification of inherent issues within the machine itself, prompting further investigation to determine the source of errors effecting the data and mitigate impact on subsequent experiments.

REFERENCE LIST

Ahrens, C. (2022). *Thermal Stress Weathering of Boulders on Airless Bodies*. [online] Available at: https://ntrs.nasa.gov/api/citations/20220005444/downloads/Ahrens.thermalstress.STI.docx.pdf.

AZO Materials (2019). *Properties: Stainless Steel - Grade 304 (UNS S30400)*. [online] AZoM.com. Available at: https://www.azom.com/properties.aspx?ArticleID=965.

Carrier, W.D., Olhoeft, G.R. and Mendell, W. (1991). Physical Properties of the Lunar Surface. *Lunar Sourcebook*, pp.475–594.

Coop, M. (2024). The 7th Bishop Lecture: The mechanics of coarse-grained geomaterials at meso- and micro-scales. *Soils and Rocks*, 47(3), pp.e2024006723–e2024006723. doi:https://doi.org/10.28927/sr.2024.006723.

Exolith Labs (2024). *Lunar Simulants*. [online] Space Resource Technologies. Available at: https://spaceresourcetech.com/collections/lunar-simulants.

Jackson, J.M., Sinogeikin, S.V. and Bass, J.D. (1999). Elasticity of MgSiO3orthoenstatite. *American Mineralogist*, 84(4), pp.677–680. doi:https://doi.org/10.2138/am-1999-0421.

Keyence (2025). *Laser Microscope VK-X Series User Support | KEYENCE America*. [online] Keyence.com. Available at: https://www.keyence.com/support/user/laser-microscope-documents/.

Malvern (2021). *Morphologi G3 particle size and particle shape image analyzer*. [online] Malvernpanalytical.com. Available at: https://www.malvernpanalytical.com/en/support/product-support/morphologi-range/morphologi-g3.

McDowell, G.R. and Bolton, M.D. (1998). On the micromechanics of crushable aggregates. *Geotechnique*, 48(5), pp.667–679. doi:https://doi.org/10.1680/geot.1998.48.5.667.

NASA (2024). *Lunar Regolith Simulant User's Guide Revision A NASA - Bing*. [online] Bing. Available at: https://www.bing.com/search?pglt=299&q=Lunar+Regolith+Simulant+User%E2%80%99s+

Guide+Revision+A+NASA&cvid=8ec5b2f71c3649c782577f8259c0a8d1&gs_lcrp=EgRlZGdlKgYIABBFGDkyBggAEEUYOdIBCDM4NzlqMGoxqAIAsAIA&FORM=ANNTA1&PC=DCTS

Noble, S. (2020). The Lunar Regolith. *NASA*. [online] doi:oai:casi.ntrs.nasa.gov:20090026015.

Schultz, R.A. (1995). Limits on strength and deformation properties of jointed basaltic rock masses. *Rock Mechanics and Rock Engineering*, 28(1), pp.1–15. doi:https://doi.org/10.1007/bf01024770.

Sun, Q., Zheng, J., Coop, M.R. and Altuhafi, F.N. (2019). Minimum image quality for reliable optical characterizations of soil particle shapes. *Computers and Geotechnics*, 114, p.103110. doi:https://doi.org/10.1016/j.compgeo.2019.103110.

Wang, W. and Coop, M.R. (2016). An investigation of breakage behaviour of single sand particles using a high-speed microscope camera. *Géotechnique*, 66(12), pp.984–998. doi:https://doi.org/10.1680/jgeot.15.p.247.